EUROPEAN ORGANIZATION FOR NUCLEAR RESEARCH

CERN-EP/99-19
1 February 1999

Measurement of Charged Particle Production from 450 GeV/c Protons on Beryllium.

The NA56/SPY Collaboration

G. Ambrosini[2)], R. Arsenescu[2)], K. Bernier[7,a)], C. Biino[5)], M. Bonesini[9)], W. Bonivento[9)], K. Borer[2)], G. Brooijmans[7,b)], M.G. Catanesi[1)], G. Collazuol[11)], D. Daniels[3)], F. Dittus[5)], K. Elsener[5)], A. Godley[13)], A. Grant[5)], G. Gregoire[7)], A. Guglielmi[11)], S. Kabana[2)], R. Klingenberg[2)], G. Lehmann[9,c)], T. Lindén[6)], L. Linssen[5)], A. Marchionni[4)], S.R. Mishra[3)], L. Moffitt[8)], U. Moser[2)], V. Palladino[10)], F. Pietropaolo[11)], K. Pretzl[2)], A. Pullia[9)], E. Radicioni[1)], S. Ragazzi[9)], J. Schacher[2)], F. Sergiampietri[12)], F.J.P. Soler[13)], F. Stoffel[2)], T. Tabarelli de Fatis[9)], F. Terranova[9)], S.N. Tovey[8)], E. Tsesmelis[5)], M. Weber[2)]

Abstract

This paper presents the results on charged particle yields and production ratios as measured by the NA56/SPY experiment for 450 GeV/c proton interactions on beryllium targets. The data cover a secondary momentum range from 7 GeV/c to 135 GeV/c and p_T values up to 600 MeV/c. An experimental accuracy on the measured yields in the range from 5% to 10%, depending on the beam momentum, and around 3% for the particle production ratios has been achieved. These measurements are relevant for a precise evaluation of fluxes and composition of neutrino beams at accelerators. Results on the target thickness and shape dependence are also reported. Inclusive invariant cross sections in the forward direction have been derived.

(Submitted to The European Physical Journal C)

[1)] INFN, Sezione di Bari, Bari, Italy.
[2)] Laboratorium für Hochenenergiephysik, Universität Bern, Bern, Switzerland.
[3)] Department of Physics, Harvard University, Cambridge, MA, USA.
[4)] INFN, Sezione di Firenze, Firenze, Italy.
[5)] CERN, Geneva, Switzerland.
[6)] Department of Physics, University of Helsinki, Helsinki, Finland.
[7)] Université Catholique de Louvain, Louvain, Belgium.
[8)] School of Physics, University of Melbourne, Melbourne, Australia.
[9)] Dipartimento di Fisica, Università di Milano and INFN, Milano, Italy.
[10)] Dipartimento di Scienze Fisiche, Università di Napoli and INFN, Napoli, Italy.
[11)] Dipartimento di Fisica, Università di Padova and INFN, Padova, Italy.
[12)] INFN, Sezione di Pisa, Pisa, Italy.
[13)] School of Physics, University of Sydney, Sydney, Australia.
[a)] Fonds pour la Recherche dans l'Industrie et l'Agriculture, Belgium.
[b)] Also Institute Interuniversitaire des Sciences Nucleaires, Belgium.
[c)] Now at Laboratorium für Hochenenergiephysik, Universität Bern, Bern, Switzerland.

1 Introduction

The NA56/SPY (Secondary Particle Yield) collaboration [1] has carried out a measurement of the production rates of charged particles from 450 GeV/c protons hitting beryllium targets of different lengths and shapes. Data have been collected over a secondary particle momentum range from 7 GeV/c to 135 GeV/c and up to 600 MeV/c transverse momentum. Previous papers have already reported on the K/π production ratios and on the production yields of charged pions measured with a 100 mm long beryllium target [2].

This paper will report final results on the production yields of charged pions, kaons, protons and antiprotons and their ratios, after a complete reevaluation of acceptance corrections and systematic errors. Yields from targets of different lengths and shapes have been measured. These results are used for deriving inclusive invariant cross sections in the forward direction.

Prior to this experiment, measurements of the pion and kaon production rates in the range 60 GeV/c $\leq p \leq$ 300 GeV/c at transverse momenta up to 500 MeV/c were performed by Atherton *et al.* [3] for 400 GeV/c protons incident on beryllium. Our data link up to and extend the earlier particle production measurements to lower secondary momenta. Comparisons will be made in the area of overlap.

Besides its general interest, the measurement of secondary particle fluxes has been mainly motivated by and is of particular importance for the understanding and planning of neutrino oscillation experiments. The calculation of the flux and energy spectra of a high energy neutrino beam is based on the knowledge of pion and kaon yields produced by protons incident on targets of materials of low atomic number. Below 60 GeV/c there has been no direct measurement of these particle production yields, and therefore extrapolations of the existing data [4] or Monte Carlo calculations [5, 6, 7] had to be used to make flux predictions.

Therefore, neutrino flux predictions are most uncertain in the low energy region, which are particularly relevant in oscillation experiments. A solid knowledge of the available secondary meson yield and of its angular distribution at low momenta is of great value for the accurate estimation of the neutrino flux at the current West Area Neutrino Facility (WANF) [8] of the Super Proton Synchrotron (SPS) at CERN, used by the neutrino oscillation experiments CHORUS [9] and NOMAD [10], where a substantial fraction of the ν_μ flux (around 50%) is due to mesons with momentum lower than 60 GeV/c, and for the planning and design of future neutrino beams [11, 12, 13, 14].

Moreover, in ν_μ beams, $\nu_\mu \mapsto \nu_e$ oscillations are usually investigated by searching for an excess of ν_e induced events with respect to the rate expected from the ν_e contamination in the beam, mostly due to K_{e3} decays. The present uncertainty in the K/π production ratio is one of the dominant sources of systematic error in $\nu_\mu \mapsto \nu_e$ oscillation searches. Below 60 GeV/c this ratio has not been measured and the predictions from the available models of particle production in proton-beryllium interactions do not agree to better than 15%.

The experimental measurements, presented in this paper, reduce the uncertainty in the ratio K/π to about 3%. The uncertainty on π or K yields is in the range of 5% to 10%, depending on the beam momentum. Inclusive invariant cross sections in the forward direction are measured with an uncertainty around 10%, in a region where data were not previously available.

2 The experimental apparatus

2.1 The H6 beam spectrometer

The NA56/SPY experiment has been performed with the NA52 spectrometer [15] in the H6 beam [16] in the North Area of the SPS (see Figure 1). The beam is derived from the T4 target station served by a primary proton beam of 450 GeV/c with typical intensities of several 10^{12} protons per burst. The beam line, with a total length of 524 m from the target, can be operated to transport secondary particles in the rigidity range 5 GeV/c $\leq p/z \leq$ 200 GeV/c (z being the particle charge). The momentum analysis is performed in the vertical plane, while the selection of the production angle is performed in the horizontal plane by means of bending magnets.

The layout of target station T4, from which three beams (H6, H8 and P0) are derived, is shown schematically in Figure 2. The direction of incidence of the primary proton beam onto the target is governed by magnets B1T and B2T. Magnets B3T and BEND1(H6) then serve to direct secondary particles of wanted sign, momentum and production angle into the H6 line, whilst deviating the remaining beam onto the dump. The production angle for the H6 beam has been varied by changing the strength

of B3T and by correspondingly correcting BEND1(H6) to put the beam on axis into the direction of H6. In this way, symmetrical production angles on either side of zero have been obtained (broken trajectories in Figure 2).

Production angles up to 15 mrad are attainable with protons impinging on the target along the beam axis, with the magnets B1T and B2T set to zero currents, as indicated in the figure. Larger production angles (up to 30 mrad) have been obtained by changing the angle of incidence of the primary beam on target, by means of the B1T and B2T magnets ("wobbling") [1].

A scan of particle flux versus production angle has been made by varying the angle of the incoming protons onto the target with B1T and B2T, to determine the accuracy of the zero-degree production angle. The maximum of this scan has been found to be within 0.1 mrad of the nominal zero-degree value.

Three sets of collimators served to define respectively the horizontal (C-hor) and vertical (C-vert) angular acceptance and the transmitted momentum bite (C-dp/p). Within a maximum acceptance of $\Delta p/p \times \Delta\Omega = \pm 1.5\% \times 2.1\ \mu$sr, they have been set to keep the trigger rate at an acceptable level [2]. In order to minimize systematic errors due to uncertainties in the field strengths of the quadrupoles, these collimators have been installed as early as possible in the beam line. For the horizontal and vertical collimators, at 41 and 48 m from the target, this implied that only two quadrupoles were located upstream of the acceptance limitation - a significant improvement over the layout used by Atherton *et al.* [3]. For the momentum slit, located at 128 m from the target, a total of six quadrupoles were involved, but only the three quadrupoles after BEND3 may affect the momentum bite.

2.2 Target station and primary beam monitoring.

In the T4 target station different targets can be brought in line with the primary beam. Data have been collected with targets made of beryllium plates of different lengths (100, 200, 300 mm), 2 mm high and 160 mm wide. This minimizes systematic effects related to possible horizontal misalignments or displacements of the primary beam and allows to study particle production at different angles for a given target thickness.

Additional data, to study the target shape dependence of secondary yields, have also been taken with a 300 mm thick target consisting of three Be rods of 100 mm length and 3 mm diameter interleaved by 90 mm of air. This target, hereafter called T9-like, is similar in structure to the one currently in use in the WANF at CERN [8]. A summary of the collected data sample is presented in Table 1.

A number of Secondary Emission Monitors (SEM) [17] located upstream and downstream of the target station and along the primary proton beam line have been used to monitor the steering of the primary protons onto the target, to record the spot size and position during the data taking period and to measure the intensity of the primary beam.

The absolute calibration of the SEMs has been performed by measuring the activation of Al foils exposed to the same beam. The Al foil response had been previously calibrated in the fast extracted beam of the WANF [8], whose absolute proton beam intensity is measured by two independent Beam Current Transformers, each one with a systematic uncertainty of 1.5%. The procedure of SEM calibration has been performed twice, before and during data taking, reaching an accuracy of 1.3% on the SEM calibration factors. The response of the SEMs has shown a stability throughout the data taking period at the $\pm 1\%$ level. The overall uncertainty on the absolute proton intensity delivered to NA56/SPY by the SPS is 1.7% [17].

The primary beam position and spot size has been monitored using the SEM profile scanners. The vertical spot size is the most critical factor in evaluating the fraction of the incident proton beam striking the target. The analysis of the beam profiles gives the fraction of incident protons hitting the beryllium plates to be 0.988 ± 0.007. Small variations in the vertical position and width throughout the experiment resulted in long term instabilities of 1%. Alternatively, all the incoming protons were hitting the T9-like target, due to its larger vertical dimensions.

To estimate the contribution to secondary particle fluxes due to the interactions of the primary proton beam with the air, the Ti vacuum windows and the Al SEM foils around the target station, runs without any target ("empty target runs") have been performed at different secondary momenta and

[1] It should be noted that these operating conditions are acceptable for the present experiment, but do not allow the use of the full acceptance of the H6 beam line.

[2] The trigger rate was always below $8 \cdot 10^3\ s^{-1}$, with typical values of $3.5 \cdot 10^3\ s^{-1}$ ($1.5 \cdot 10^3\ s^{-1}$) at 135 (40) GeV/c.

production angles. Added together these materials represent 0.6% of an interaction length. The empty target yield provides a fairly constant correction of the order of 3% to 4% to the 100 mm target data and of 1.5% to the 300 mm target data. This corresponds to an equivalent target length of 2.8 mm of beryllium, corresponding to 0.68% of an interaction length, in rough agreement with the expectation. The correction factor is slightly dependent on the beam momentum and on the type of the secondary particles considered and gives a negligible contribution (less than 0.1%) to the systematic uncertainty on the particle production yields.

2.3 Detector description

Particle identification is provided by a set of time of flight (TOF1-5) detectors, threshold (C0,C1,C2) and differential (CEDAR) Cherenkov counters along the beam line and a hadron calorimeter at its end. Additional scintillator counters (B0,B1,B2) in the beam line are used for trigger purposes and further timing information. A set of proportional chambers (WnT,(n=1,5), WmS,(m=2,3)), with a 3 mm wire spacing, tracks particles through the spectrometer (see Figure 1). The relevant detector characteristics are shortly reviewed hereafter.

TOF1-5 are scintillator hodoscopes which provide the measurement of the particle speed. Each hodoscope covers a maximum beam aperture of 10×10 cm^2 and is made of 8 vertical scintillator slats with a thickness of either 1 cm (TOF1, TOF3 and TOF5) or 0.5 cm (TOF2 and TOF4). The measured intrinsic time resolution is 74 ± 1 ps for the 1 cm thick and 100 ± 1 ps for the 0.5 cm thick TOF counter hodoscopes [15].

Two Cherenkov counters (C0 and C1), located at 258 and 268 m from the target, have a common gas control, but separate readout. They have been filled with N_2 gas, which provides π/K separation up to 20 GeV/c and K/p separation above 20 GeV/c. A third counter (C2), located at 505 m from the target, has been filled with He gas to allow for e, μ rejection at 15 and 20 GeV/c and provide π/K separation above 20 GeV/c. The gas fillings have been chosen in order to complement the particle identification capabilities of the TOF system.

A Cherenkov Differential counter with Achromatic Ring focus (CEDAR-N) [18] was placed in the H6 beam line at 440 m from the target. The CEDAR pressure has been always set to flag pions in order to reinforce the π/K separation. This is particularly important at high momenta (67.5-135 GeV/c), where the detection efficiency for pions in the Cherenkov counters is not optimal.

A hadron calorimeter, consisting of five uranium/scintillator modules for a total depth of seven interaction lengths, is located at the end of the spectrometer (539 m downstream of the target). It has electromagnetic and hadronic energy resolutions of $\sigma_E^{em}/E = 0.174(GeV^{1/2})E^{-1/2} \oplus 0.009$ and $\sigma_E^{had}/E = 0.356(GeV^{1/2})E^{-1/2} \oplus 0.028$ [15], respectively. Its longitudinal segmentation allows for an effective separation of electrons from hadrons, as shown in Section 4. Muons are identified requiring an energy deposition consistent with that of a minimum ionizing particle.

2.4 Trigger and data acquisition.

The trigger is based on two independent trigger signals formed at 268 m (trigger A=TOF2·B1) and 505 m (trigger B=TOF4·B2) downstream of the target. In addition, the information of the threshold Cherenkov counters are used in anti-coincidence to veto or downscale particles above threshold. The inclusion of the Cherenkov counters in the trigger definition is conditioned by the status of a logic level (*Cveto*): when $Cveto = 0$, all the particles are triggered independently of the Cherenkov counter information; when $Cveto = 1$, only heavy particles (below Cherenkov threshold) generate a trigger signal.

Since the rate of pions in the spectrometer has been always much larger than the rate of kaons, pions and lighter particles have been downscaled at the trigger level to enrich the relative K content of the collected sample. In the adopted downscaling logic the status of the *Cveto* level has been flip-flopped at each event readout. In this way, one half of the collected triggers, spill by spill, reflects the natural beam composition, while the remaining half contains only kaons and protons.

The read out and data acquisition system is also divided into two separate sections A and B, according to the trigger scheme. The upstream system reads out all detectors up to TOF3 (see Figure 1). The remaining detectors are read out by the downstream section. The two independent data acquisition sections are synchronized by a trigger controller, which ensures that a local trigger in either section is accepted only if it does not fall within a dead-time period of the other. Two different operating modes are

permitted by the trigger controller. In the first, events are required to have triggered both trigger A and B (mode A·B). In the second, only trigger A is required, providing higher detection efficiency for short lived particles, which decay before reaching the downstream end of the spectrometer. The downstream detectors are read out only if trigger B fires as well.

The number of hits for each component of the trigger has been recorded at each spill by the data acquisition system. This information has been used to compute the system deadtime and to monitor the trigger efficiency for each run.

The efficiency of the coincidence TOF2·B1 is measured from the ratio of the four-fold coincidence (TOF2·B1)·(TOF4·B2) to the coincidence TOF4·B2. This efficiency is 0.986 ± 0.001 and is stable throughout the data taking period. Corrections for trigger inefficiencies in section B of the experimental apparatus are folded in the correction for particle losses along the beam line, which has been measured with proton runs (see Section 3.1).

The DAQ livetime corrections are measured from the scalers as the ratio of the acquired triggers to the total number of triggers. Corrections for trigger pileup have been also evaluated on the basis of the single rate in each detector and accounted for in the livetime correction factor. Due to the adopted trigger logic with the downscaling of light particles, the DAQ livetime at intermediate and high momenta (from 15 to 135 GeV/c) is different for different particles: while heavy particles have been always generating an acceptable trigger, light particle triggers have been accepted only if *Cveto* was off. Protons, which are abundant in both the *Cveto-on* and the *Cveto-off* samples, have been used to check for systematic effects in the livetime correction. Systematic effects larger than 0.1% have been excluded.

3 Beam line acceptance and particle transport.

3.1 Acceptance and transmission evaluation.

The acceptance of the spectrometer is represented as the product of a phase-space acceptance times a transmission coefficient $\mathcal{T}$, which accounts for particle losses along the beam line:

$$\mathcal{A} = \Delta\Omega \cdot (\frac{\Delta p}{p}) \cdot \mathcal{T} \tag{1}$$

The geometrical acceptance $\Delta\Omega$ and the transmitted momentum bite $\Delta p/p$ are defined by the openings between the jaws of three collimators. To ensure an acceptable trigger level, two sets of collimator openings have been chosen, for $p \leq 40$ GeV/c and $p > 40$ GeV/c.

The system that sets the collimator aperture scale has been calibrated in the laboratory prior to installation in the beam tunnel. The opening scale of each collimator has been tested at the beginning of the experiment in a number of dedicated runs at 135 GeV/c, in which the flux of secondary protons has been measured as a function of one collimator opening, the other two remaining fixed. All the three collimators have shown the expected linear behaviour. However, for the two collimators defining the horizontal (C-hor) and vertical (C-vert) acceptance an intercept at zero flux not consistent with a null opening has been measured (C-hor $= -0.44 \pm 0.18$ mm and C-vert $= -1.34 \pm 0.16$ mm). The third collimator has been found to have an offset consistent with zero (C-dp/p$=-0.03 \pm 0.10$ mm). These results have been interpreted as due to openings between the jaws of the first two collimators larger than the read out nominal values, by an amount equal to the measured offsets and have been confirmed by a mechanical inspection after the end of the experiment. From the above, the geometrical acceptance of the spectrometer is estimated to be $(16.53 \pm 0.54) \times 10^{-3}$ μsr ($\Delta p/p\%$) for momenta $p \leq 40$ GeV/c and $(3.22 \pm 0.19) \times 10^{-3}$ μsr ($\Delta p/p\%$) above 40 GeV/c.

Particle transmission along the beamline is computed with an improved version of the TURTLE Monte Carlo simulation [19], which includes multiple scattering and nuclear interactions in the detector and beamline material (about 20% of a nuclear collision length in total, with a 10% uncertainty). Data on nuclear cross sections from references [20, 21] have been parametrized to model the nuclear interactions as a function of particle type and momentum [3]. Because of their different nuclear cross-sections, different

[3] In the parameterization of nuclear interactions, data from reference [20] have been used in the momentum region $p \geq 60$ GeV/c. At lower energies measurements are available only from reference [21], which shows a $\sim 14\%$ higher value in absolute cross section with respect to data from reference [20] in the region of overlap (around 60 GeV/c). So, for momenta lower than 60 GeV/c only the shape of the measurements from reference [21] has been used while keeping the normalization of absolute cross-sections from reference [20].

transmissions are obtained for the different particles ($\pi^{\pm}, K^{+}, K^{-}, p, \overline{p}$). In addition, the transmission for protons in the second part of the spectrometer (downstream of B1) has been measured at various momenta and collimator settings with special proton runs, in which trigger A alone was required with the C0 and C1 counters in anticoincidence to veto particles lighter than protons.

The TURTLE simulation is more accurate in the first part of the beam line (up to B1), where the beam profiles in the wire chambers are well reproduced (see Figure 3). Moreover, for $p \geq 15$ GeV/c the transmission upstream of B1 was not limited by the physical apertures of the beam magnets. The beam profiles observed at TOF2, where the beam had maximum size in the first part of the apparatus, are well within the transverse apertures of all the beam line elements. The systematic uncertainty of the calculation of the transmission up to B1 has been estimated by changing various parameters of the simulation. In particular, the field strengths of all the quadrupoles in the first part of the beam line have been allowed to vary according to the uncertainty in the supplied current. This results in an uncertainty in the transmission ranging from 8% at 7 GeV/c to 4% at 15 GeV/c and to 1.5% at 40 GeV/c.

The transmission measured in proton runs in the second part of the beam line is always lower than the expectations. Once the efficiency of trigger B ($\epsilon_B \simeq 97\%$) is taken into account, a discrepancy ranging from 2% at $p \geq 40$ GeV/c to 8% at 15 GeV/c has been found [4] (see Figure 4). This discrepancy mainly originates in the last part of the beam line (downstream of TOF3), where broader beam profiles are observed in data than in Monte Carlo. Beyond TOF3, in particular at low momenta, the transmission is limited by the physical aperture of the magnets along the beam line and the calculation of the particle loss critically depends on the exact treatment of edge effects in the fields of the magnets and on magnet misalignments. Results on the acceptance studies and on the comparison between proton data and TURTLE predictions are reported in Table 2, which lists as an example the acceptances for pions and protons in the adopted running conditions. Column 2 gives the acceptances at B1 calculated as $\mathcal{A}_A = \Delta\Omega \cdot (\Delta p/p) \cdot \mathcal{T}_A$; column 3 the calculated transmission $\mathcal{T}_{\mathcal{B}}$ from B1 to the calorimeter; column 4 lists the ratio of the measured proton transmission downstream of B1 to the TURTLE prediction.

Transmissions in the final part of the beam line have been monitored and found to be stable using several proton runs taken over the whole period. To account for the discrepancy between data and simulation, the transmissions predicted for particles from B1 to the end of the spectrometer have been scaled according to the observed losses in the corresponding proton data, using the formula:

$$\mathcal{A}^{\pi,K,p} = \mathcal{A}_A^{\pi,K,p} \cdot \mathcal{T}_B^{\pi,K,p} \cdot \frac{\mathcal{T}_B^{p,data}}{\mathcal{T}_B^{p,Turtle}} \tag{2}$$

A systematic error of order 1% is attributed to this procedure to account for the uncertainty in the measurement of the proton transmission. An additional systematic error equal to the observed discrepancy between TURTLE and the measurement has been added in quadrature, reflecting a conservative choice in the estimate of the error on the beam line acceptance [5]. In conclusion, the spectrometer acceptance has been derived with an accuracy between 5% and 10% depending on the beam momentum, dominated by the accuracy of the phase-space acceptance at high momenta and of the beam line transmission at low momenta.

In the measurement of same sign particle production ratios the uncertainties related to the acceptance definition (magnet strengths, collimator openings, etc.) cancel, and only the particle dependence of the transmission along the beam line has to be accounted for. The systematic contribution coming from this correction on the measurement of particle production ratios is of the order of 1%, due to uncertainties on the amount of material along the beam line and on the nuclear cross sections.

At 7,10,15,40 and 67.5 GeV/c, the production ratios of opposite sign particles can be derived from the measurements of opposite sign particle yields. Also in this case the error related to the definition of the phase-space acceptance cancels, except for the measurements at 67.5 GeV/c, where two set of collimators openings, corresponding to the same nominal phase-space acceptance, have been used for positive and

[4] Note that in the measurement of the particle fluxes at 7 and 10 GeV/c, particles were not tracked downstream of B1.

[5] It must be emphasized that if we had instead used the absolute nuclear cross section values from reference [21] to parametrize nuclear interaction effects in the simulation, the discrepancy between measured and simulated proton transmissions would be reduced. The still remaining discrepancy in the final part of the spectrometer is attributed to geometrical effects. In this way, the choice of the absolute cross-sections values from reference [20] makes us confident that the quoted systematic errors on transmission are not underestimated.

negative particles.

3.2 Correction for particle decay and determination of the beam momentum.

Since pions and kaons are tagged after several decay lengths from the target, an accurate determination of decay corrections is always relevant and in particular for a precise measurement of the K/π ratio, where other sources of systematic errors are strongly reduced. To accomplish this, the raw yields of secondary mesons are multiplied by a factor given by:

$$f_\tau = \exp(\frac{L}{pc}\frac{mc^2}{c\tau}); \tag{3}$$

where $c\tau/mc^2 = 7.51$ m/GeV for kaons and 55.9 m/GeV for pions; L is the distance between the target and the point where the particles are detected and p is the beam momentum. The relative uncertainty on the decay correction due to the uncertainty Δp on the measurement of the beam momentum and $\Delta(c\tau/mc^2)$ on the particle mean flight path is given by [6]:

$$\frac{\Delta f_\tau}{f_\tau} = \frac{L}{pc}\frac{mc^2}{c\tau} \times (\frac{\Delta p}{p} \oplus \frac{\Delta(c\tau/mc^2)}{(c\tau/mc^2)}), \tag{4}$$

and is proportional to the number of decay lengths $(L/pc)(mc^2/c\tau)$. The total length of the spectrometer corresponds to 4.8 (3.6) decay lengths for kaons of 15 (20) GeV/c. At 7 (10) GeV/c kaons were tracked only in the upstream part of the spectrometer, corresponding to 5.1 (4.9) K decay lengths.

The K lifetime is known with a relative precision of 0.2% [22], which limits the precision on $\Delta f_\tau/f_\tau$ to about 1% at low momenta. A knowledge of the absolute beam momentum with a precision of order 10^{-3} is then required at low momenta to keep the error on $\Delta f_\tau/f_\tau$ at the percent level.

By exploiting the resolution of the TOF system, the beam momentum can be derived with the required precision from the difference in the time needed by particles of different mass to travel the same distance:

$$m^2c^4 = (pc)^2\frac{2\Delta t}{t_0} \tag{5}$$

where $t_0 = d/c$ is the time of flight of $\beta = 1$ particles over the distance d, m is the particle mass and Δt is the time delay of massive particles with respect to t_0.

At 7 and 10 GeV/c only the upstream part of the spectrometer (from TOF1 to TOF3) can be used to measure the beam momentum. An example, at 10 GeV/c, is shown in Figure 5. This method is then used to individually correct runs taken at nominal momenta of $\pm 7, \pm 10$ GeV/c. The error on the fitted momentum is typically less than 10 MeV/c for each run, giving a systematic contribution to the decay correction factor below 0.5%.

At intermediate momenta (15 and 20 GeV/c), particles have been tagged at the calorimeter, at the end of the beam line. For consistency checks, two independent estimates of the beam momentum have been obtained from the time of flight in part A of the spectrometer (from TOF1 to TOF3) and in part B (from TOF4 to TOF5). Figure 6 shows the correlation of the two beam momentum estimates for runs at 15 GeV/c. Four clusters of estimated momenta are visible, corresponding to four different beam tuning conditions at 15 GeV/c throughout the NA56/SPY data taking period. Some remarks are in order: i) the beam momentum spread between runs in the same beam conditions is compatible with the estimated precision of the method (a few MeV/c); ii) the beam momentum is reproducible within about 100 MeV/c. A common decay correction factor is used in the analysis for all the runs taken with the same beam tuning, by averaging the momentum estimate over those runs. The relative error on the estimated beam momentum is less than 0.1% both at 15 and 20 GeV/c. This translates into a negligible contribution to the uncertainty in the decay correction at intermediate momenta.

At high momenta, particle decay lengths are longer and decay corrections are less important. Although at 30 and 40 GeV/c the precision of the time of flight measurement is worse (about 100 MeV/c), it is still sufficient to keep the systematic uncertainty related to the K decay correction below the one percent level. At even higher momenta, the beam momentum as measured from the magnet

[6] The contribution of $\Delta L/L$ to the error is negligible.

strengths has to be used. This gives an accuracy of around 500 MeV/c, which translates into a systematic error on the decay correction for kaons of 0.8% (0.2%) at 67.5 (135) GeV/c.

Decay corrections given by equation (3) are valid if all the mesons decayed upstream of the last detector considered in the analysis (B1/TOF3 or the hadron calorimeter) are either lost or rejected by the analysis selection criteria. However, particles produced in K and π decays might have been transported and have faked a good signal in the apparatus. This background is evaluated with a Monte Carlo simulation of meson decays and transport of the decay products along the beam line, and subtracted from the selected pion and kaon sample. At 7 and 10 GeV/c, this introduces a correction of a few percent on π and K yields and a negligible correction on K/π. At higher momenta, where only particles associated to an hadronic shower in the calorimeter are selected by the data analysis, the correction is zero for pions and of a few percent for K yields and the K/π ratio. The associated systematic error is of the order of 0.1%.

4 Data analysis.

Data have been collected in a momentum range of secondary particles from 7 to 135 GeV/c. The trigger configuration and detector setup have been varied depending on the beam momentum in order to optimize the particle identification capabilities and the detection efficiency.

The π flux (p flux for momenta ≤ 10 GeV/c) and the p/π and K/p production ratios are separately extracted from the all particle unbiased sample (i.e. *C-Veto off*) or the heavy particle sample (i.e. *C-Veto on*), while the ratio K/π and the other fluxes are derived quantities. This approach makes the measurement of the particle production free from any possible bias related to different experimental configurations between light and heavy particles.

The K/π production ratio is evaluated taking into account corrections for empty target subtraction, particle decays and nuclear interactions of secondary particles along the beam line in the measurements of (K/p) and (p/π). Relevant contributions to the systematic error come from the particle decay correction ($\sim 1\%$), the nuclear interaction correction ($\sim 1\%$) and the empty target subtraction ($\sim 0.2\%$).

To extract π flux (or p flux for momenta ≤ 10 GeV/c) from the data, corrections for selection efficiency, primary beam intensity, phase-space acceptance and transmission, particle decays, DAQ livetime, trigger efficiency and empty target flux have been applied. The precision of these results is limited by the error on the spectrometer acceptance, which is by far the largest contribution to the total error.

4.1 Analysis at low momenta

At low secondary momenta (7 and 10 GeV/c), trigger A alone has been required in order to increase the detection efficiency for short lived particles. The trigger has been defined by $A = B1 \cdot TOF2 \cdot \overline{(C0 + C1)}$. Data taking has been accomplished in two separate steps by setting the pressure in the C0-C1 counters to veto particles lighter than pions in one case (runs A_L) and lighter than kaons (runs A_H) in the other case. The latter setting has been adopted to increase the kaon statistics in the collected sample and to reinforce the π/K separation provided by the TOF system.

Data from runs A_L are used to measure the p/π production ratio, while data from runs A_H are used to measure the K/p production ratio. The proton yield is measured from the combined runs A_L and A_H. As mentioned above, the K/π ratios and the π and K yields are derived quantities. The adopted trigger configuration and analysis procedure has ensured a statistical accuracy on the K/π production ratios of 3% at 10 GeV/c and 4% at 7 GeV/c, dominated by the statistics of the K sample collected in runs A_H.

In runs A_L, electrons and muons are rejected at the trigger level by a signal both in the C0 and the C1 counters. At 7 GeV/c the Cherenkov veto was fully efficient both to electrons and muons; at 10 GeV/c the inefficiency to muons was below 0.5%. The residual contamination in the pion sample (runs A_L) is negligible at 7 GeV/c and below 10^{-3} at 10 GeV/c. This last conclusion depends on the knowledge of the μ/π ratio in the beam (below 10%), which has been estimated from a pressure scan performed with the C2 counter at 15 GeV/c (see Figure 7).

These considerations only apply to muons within the beam acceptance. However, an additional background due to off-momentum muons of the beam halo, which triggered the apparatus being outside of the C0-C1 acceptance, was also present both in runs A_L and A_H. This background is rejected in data analysis at 10 GeV/c by tagging particles at TOF3, where off-momentum muons are not transmitted owing to the momentum recombination operated by BEND5 (see Figure 1). The quality of the particle

identification in the 10 GeV/c data sample selected at TOF3 is demonstrated in Figure 8: pions are well separated from heavier particles in runs A_L, with a small contamination from kaons (less than 0.1 %); the contamination from pions and from off-momentum muons in the kaon sample is negligible in runs A_H.

At 7 GeV/c, particles are only required to reach B1, since longer distances would have degraded the K content of the beam and the resolution of the TOF system was already good enough to allow for the rejection of the small off-momentum muon background in runs A_H. The off-momentum muon background in the π sample of runs A_L is estimated to be negligible on the basis of the observed background in runs A_H. For negative particles at 7 GeV/c no data have been collected with the C0-C1 veto for particles lighter than kaons and the π/K separation has to rely only on the TOF system. This gives an additional systematic error of 7% in the estimation of the K yield and of the K/π ratio, due to the π contamination in the K sample. Otherwise, the systematic error due to particle identification is negligible.

Since protons are well separated in mass from lighter particles, at both 7 GeV/c and 10 GeV/c, the proton yield is measured at B1, to reduce the uncertainty on the acceptance evaluation related to the transmission downstream of B1. The efficiency of the coincidence $B1 \cdot TOF2 \cdot \overline{(C0 + C1)}$, used to define the trigger and relevant for the measurement of absolute particle yields, has been estimated with an accuracy of a few tenths of a percent from the efficiency of $TOF2 \cdot B1$ (see Section 2.4) and the probability that a good trigger has been vetoed by light particle pileup or random noise in either of the Cherenkov counters. Discrepancies up to 4% have appeared in the proton yields computed from runs A_L and runs A_H both at $\pm$10 GeV/c and $\pm$7 GeV/c. We quote as proton yield their weighted average and include the observed discrepancy in the quoted systematic error.

4.2 Analysis at intermediate momenta.

At 15 GeV/c and 20 GeV/c, the coincidence of both triggers (A·B) has been required and the trigger has been defined by:

$$\begin{aligned} \mathrm{A} &= \mathrm{B1} \cdot \mathrm{TOF2} \cdot \overline{(\mathrm{C0{+}C1}) \cdot \mathit{Cveto}}, \\ \mathrm{B} &= \mathrm{B2} \cdot \mathrm{TOF4} \cdot \overline{\mathrm{C2}}. \end{aligned}$$

The C0–C1 counters have been used to prescale pions, while the C2 counter has been operated about 200 mbar below the π threshold, in order to veto electrons and muons (see Figure 7).

The efficiency of the electron veto has been checked using the calorimeter information and the residual background has been found negligible. Moreover, in the data analysis, particles have been tagged at the calorimeter by requiring an energy deposition consistent with the expectations for hadrons. This has reduced the muon background coming from meson decays downstream of C2 and from the small C2 inefficiency to muons to a negligible level.

The proton identification completely relies on the time of flight measurement. For the full sample of the events collected, a mass hypothesis has been formed from the measurement of the particle speed on the basis of the available hits in the TOF hodoscopes and in the trigger counters. The mass resolution achieved at 15 GeV/c and 20 GeV/c is shown in Figure 9. At both momenta, protons are identified with full efficiency and negligible contamination requiring $0.5 \leq m^2 \leq 1.5$ GeV$^2/c^4$.

The π/K separation relies on the C0, C1 and CEDAR counters. The latter has been set to flag pions, in order to reinforce the separation provided by the C0–C1 counters. The pulse height spectra observed in C0 and C1 in a typical run at 15 GeV/c are shown in Figure 10 for the full sample of particles and for identified protons. Tails at large pulse heights, visible in the proton sample, are due to the pileup of a light particle within the charge integration time of the ADC. A small fraction of events with pileup in both Cherenkov counters is also visible.

The p/π production ratio and the pion flux have been measured from the sample of events collected with the trigger condition *Cveto-off*, which reflected the natural beam composition. Protons have been separated from lighter particles on the basis of the mass hypothesis; kaons have been rejected from the pion sample by requiring light in C0 and C1 as indicated in Figure 10. The inefficiency of this selection has been measured with a clean control sample of pions tagged by combining CEDAR and TOF information and has been found to be $1 - \epsilon_\pi = (1.1 \pm 0.4) \times 10^{-5}$ at 15 GeV/c and $1 - \epsilon_\pi = (5.7 \pm 1.3) \times 10^{-4}$ at 20 GeV/c. The size of the kaon background in the pion sample has been estimated from the probability that particles identified as protons by the mass hypothesis satisfy the pion selection. The misidentification probability has been measured to be at the percent level, limited by pileup of light particles in both the

Cherenkov counters. This, combined with a typical K/π ratio of 10^{-3} at the end of the spectrometer, ensures that the kaon background in the pion sample is negligible.

The measurement of the p/π production ratio has a statistical accuracy of about 1%, limited by the proton statistics in the *Cveto-off* sample. The systematic error is at the percent level, with the main contributions coming from the uncertainty on the particle transmissions due to the difference of the proton and pion nuclear cross-sections ($\sim 1\%$) and the empty target subtraction ($\sim 0.2\%$). The statistical error on the pion flux is less than 1%, while the main contribution to the systematic error comes from the uncertainty on the spectrometer acceptance (see Section 3).

In the measurement of the K/p ratio, heavy particles have been selected by requiring a pulse height consistent with the pedestal both in the C0 and the C1 counters and that the particles have not been flagged as a pion by the CEDAR counter. By exploiting the redundancy of the Cherenkov counters and TOF system, the pion misidentification probability has been measured to be less than 10^{-5}. The additional requirement that the mass hypothesis be larger than $< m_K^2 > -5\sigma(m^2)$ has reduced the pion contamination in the kaon sample to a negligible level. These criteria for pion rejection do not bias the K/p measurement, since they are equally inefficient for kaons and protons. In the heavy particle sample, a K/p separation with full efficiency and purity has then been achieved according to the mass hypothesis.

The K/p production ratio has been measured independently from both samples collected with the *Cveto-off* and *Cveto-on* trigger conditions and the measurements have been combined. The precision in the measurement of the K/p ratio is dominated by the sample collected with the *Cveto-on* condition (about 10^3 kaons and 10^5 protons), which sets the statistical accuracy on the K/p ratio to the 3% level. The main contributions to the total systematic error are related to the corrections for K decays along the beam line (0.9% at 15 GeV/c and 0.7% at 20 GeV/c), for nuclear interactions ($\sim 1.5\%$) and for the empty target subtraction ($\sim 0.2\%$).

The K/π production ratio is derived from the previously mentioned production ratios as $(K/\pi) = (K/p) \cdot (p/\pi)$, with a statistical uncertainty of 3% due to the K/p measurement. Similarly, the K and p yields are derived from the π yields and the K/π and p/π production ratios.

4.3 Analysis at high momenta

At high momenta (above 20 GeV/c), the TOF resolution is not sufficient for a clean $\pi/K/p$ separation, therefore all Cherenkov counters in the beam line have been devoted to this purpose. In particular, C2 has been used for π/K separation and for π and lighter particles prescaling at the trigger level, while K/p separation has been performed with C0 and C1. However, the latter two counters are not conditioning the trigger, which has been operated in the A·B mode, with:

$$\begin{aligned} \mathrm{A} &= \mathrm{B1} \cdot \mathrm{TOF2} \\ \mathrm{B} &= \mathrm{B2} \cdot \mathrm{TOF4} \cdot \overline{\mathrm{C2} \cdot \mathit{Cveto.}} \end{aligned}$$

Redundant information on the π/K separation is provided by the CEDAR counter, that has allowed to reinforce pion identification especially at 67.5 and 135 GeV/c.

In the data analysis, particles have been tracked along the beam line requiring one hit in each TOF hodoscope, resulting in a reconstruction efficiency of 0.976 ± 0.003. Particles have been tagged at the calorimeter requiring an energy deposition consistent with what expected for an hadron. As seen in Figure 11, electrons and muons are easily rejected: electrons deposit all their energy in the first module of the calorimeter, 45 radiation lengths long; muons give a signal consistent with a minimum ionizing particle, $E_{m.i.p} \simeq 0.5$ GeV in each module of the calorimeter. The efficiency of the calorimetric selection for hadrons has been estimated to be 0.995 ± 0.001 from data and a dedicated simulation, based on the GEANT package [5]. From this simulation the charge-exchange processes in the calorimeter, that may be a source of misidentification for pions and kaons, have been found to be at a negligible level (around 10^{-3}).

Due to the adopted Cherenkov settings, pions are expected to give signals in all the Cherenkov counters (C0,C1 and C2 , CEDAR) while kaons give signals only in counters C0-C1. Protons are identified as being always below threshold in all Cherenkov counters. In order to avoid pileup and the occurrence of spurious signals in the $\sim$ 100 ns charge integration window of ADCs, the measured pulse-height of the Cherenkov counters (C0,C1 and C2 ,CEDAR) have been correlated to the timing information from their corresponding TDCs. Events are considered in-time if they are within a few nanoseconds from the reference signal of the trigger (see Figure 12). The C0-C1 and C2 pulse height spectra, observed in a

typical run at 40 GeV/c, are shown in Figure 13.

Due to the redundancy of information available at each energy, it has been possible to measure the efficiencies and contaminations for particle identification. Particle identification is always fully efficient, except at 135 GeV/c where a 2%(3.4%) inefficiency has been found for $\pi(K)$. The contamination level is below 10^{-4} in the pion sample and ranges from $5 \cdot 10^{-3}(10^{-5})$ to $0.28(4 \cdot 10^{-3})$ in the $K(p)$ sample from 30 to 135 GeV/c. The sizeable π contamination in the kaon sample at 135 GeV/c comes from the measured 2% inefficiency of C2 and CEDAR to pions, at this momentum. The small inefficiency of the K identification at 135 GeV/c results anyhow in a negligible contamination in the proton sample. Systematic uncertainties on the particle identification and the analysis procedure are about 0.1% for pions and protons and less than 1% for kaons.

The p/π production ratio is measured from the sample of events collected with the trigger condition *Cveto-off*. The K/p production ratio is measured independently from both the sample collected with the *Cveto-off* and *Cveto-on* trigger conditions and the results have been combined. The K/π ratio as well the K and p production yield are then derived as before. The prescaling of the light particles has allowed a statistical uncertainty smaller than 1% (2%) for the determination of pion and proton (kaon) yields, while the production ratios are always measured with statistical uncertainty smaller than 2%. The systematic uncertainty on the ratio K/π is never greater then 1.5% and comes mainly from nuclear interaction corrections and systematics on kaon identification.

5 Experimental results

5.1 Particle yields and production ratios

Secondary particle yields Y are given by:

$$Y(p,\theta) = \frac{N(p,\theta) \cdot C(p,\theta)}{I \cdot \mathcal{T}(p) \cdot (\Delta p/p\%)\Delta\Omega} \tag{6}$$

where $N(p,\theta)$ is the measured number of events at momentum p and at angle θ, $\mathcal{T}(p)$ the beam line transmission as computed in Section 3.1, $(\Delta p/p)\Delta\Omega$ $[\% \cdot sr]$ the spectrometer acceptance, I the total number of protons on target and $C(p,\theta)$ a factor that takes into account all corrections illustrated in Section 2 and 3.

In addition, $N(p,\theta)$ for pions and protons is corrected for contributions from strange particle decays (K^0_s, Λ^0, $\Sigma^{\pm}$,...) outside the target. These may be important, especially at low momenta, due to the 1.35 m distance between the target station and the first bending magnet in the H6 beam line. A full simulation of the beam target area has been implemented using the GEANT package with the FLUKA generator [5], to compare the yields of pions produced inside the target with those coming from K^0_s or Λ^0 decays outside the target. Results have been cross-checked with a fast generator, in which pions from K^0_s decay have been generated within our experimental acceptance, transported along the beam line and weighted according to the parent K^0_s production cross-section [7)]. The two calculations agree within 20%. An additional systematic uncertainty of 10% to the pion contribution is attributed to the contributions of $\Sigma^{\pm}$ and $\overline{\Lambda}$ decays, neglected in both models. The estimated contamination are in the range from 4.8% (8.6%) at 7 GeV/c to 1.2% at 135 GeV/c for positive (negative) pions in the forward direction and decreases as a function of the production angle. An overall uncertainty of 25% on the knowledge of this contamination has been assumed. The contamination of the proton (antiproton) sample, due to $\Lambda \mapsto p\pi^-$ ($\overline{\Lambda} \mapsto \overline{p}\pi^+$) decays is estimated in a similar way. It goes from 14.4% (8.1%) at 7 GeV/c to 2.1% (3.6%) at 135 GeV/c (67.5 GeV/c) in the forward direction. As before, an overall uncertainty of 25% has been assumed.

In the following, results are reported for the 100 mm Be plate target on secondary particle yields ($\pi^{\pm}$, $K^{\pm}$, p, $\overline{p}$) and particle production ratios (K/π, p/π, K/p) in the forward direction, as a function of the secondary particle momentum. For simplicity, results are given at their nominal beam momentum in all tables and figures, while the measured momenta (see Section 3.2) are shown in Table 3. For secondary momenta of 15 and 40 GeV/c, yields and particle production ratios as a function of the transverse momentum, as determined from the production angle, are also shown for the 100 mm Be plate target.

Particle yields and ratios are given in the tables both corrected for strange particle decays outside the target and before this correction (in parentheses). The latter values might be of use for beam line

[7)] The K^0_s production cross-section was evaluated from our measurements of the K^+ and K^- fluxes, according to $N_{K^0_s} = \frac{1}{4}(N_{K^+} + 3 \cdot N_{K^-})$ as suggested by [24].

configurations where the distance between the target and the first beam element is of the same order as in our experimental setup (1.35 m). Particle yields and production ratios shown in the plots are always corrected for strange particle decay contamination outside the target.

5.1.1 Beam momentum dependence

Results on particle yields and production ratios in the forward direction as a function of beam momentum are listed in Tables 4 to 7 and shown in Figures 14 and 15. The systematic and statistical errors have been added in quadrature.

As discussed above, the dominant systematic error in the evaluation of particle yields is due to the acceptance calculation: it ranges from 5% at high momenta to 10% at low momenta. Systematic errors on production ratios are instead mainly due to particle decay corrections for K ($\leq 1\%$) and to the evaluation of the transmission along the beam line ($\sim 1\%$), which is particle dependent.

Results obtained by Atherton *et al.* [3] are also shown in the plots. Since the primary beam in our experiment (450 GeV/c) had higher momentum than the one of Atherton *et al.* (400 GeV/c), the Atherton measurements at 60 and 120 GeV/c, corresponding to the same $x_F = p_L/p_{inc}$ as our measurements at 67.5 and 135 GeV/c have been reported in the figures at momenta $p = 67.5$ and 135 GeV/c. Moreover, their particle yields have been rescaled by $(450/400)^2$, on the basis of the relation between the invariant cross-section and the yields as given in the figures. It should be stressed that the Atherton *et al.* data, shown in the plots, are not corrected for strange particle decays. Owing to the similarity of the spectrometers, these corrections can be estimated to be of the same order as in our experiment. Taking this into account, the results of the two experiments are everywhere in agreement within 1.6 σ.

5.1.2 Angular dependence

Angular scans have been performed at 15 and 40 GeV/c, with an uncertainty on the secondary production angle of about 0.1 mrad. In order to check the precision of the selected production angle, some of the measurements have been repeated at symmetric angles. Since compatible results were always obtained, they have been combined. Results are shown in Tables 8 to 13 and Figures 16 to 17.

The systematic error quoted on particle yields accounts only for run dependent systematic uncertainties. It includes the uncertainty on the long term stability of the SEM calibration factors for the measurement of the primary beam intensity ($\sim 1\%$), instabilities in the steering of the primary proton beam on the target ($\sim 1\%$) and the uncertainty of the DAQ livetime correction ($\sim 0.1\%$). The systematic error common to all the points on the angular scan (and not shown in the plots) amounts to 10% at 15 GeV/c and 5% at 40 GeV/c. This takes into account contributions from the uncertainties on the acceptance calculation, the SEM absolute calibration and the particle decay correction (0.9% for kaons and 0.2% for pions at 15 GeV/c). The contributions from the trigger efficiency correction and the empty target flux subtraction are negligible.

Most of the sources of systematic errors on the production ratios are common to all points of the angular scans, except the correction for strange particle decays, that decreases with the transverse momentum. Common systematic errors, not listed in the tables and not included in the plots, amount to $1.3\%, 1.1\%, 1.7\%$ at 15 GeV/c and $1.1\%, 1.1\%, 1.5\%$ at 40 GeV/c for K/π, p/π, K/p respectively. The p_T distributions, measured at 15 and 40 GeV/c, do not support the assumption of scaling invariance for the p_T dependence.

5.2 Target thickness dependence

At $+10, +15, \pm 40$ GeV data have been taken with beryllium plate targets of different lengths (100 mm, 200 mm and 300 mm) at 0 mrad. Additional data were also taken with the T9-like target, which in the forward direction is equivalent to the plate 300 mm Be target.

In a naive absorption model, where the produced secondaries if absorbed in the target do not generate additional particles, the target production efficiency $f(L)$ for secondary pions or kaons (denoted by s in the following) is given by [4]:

$$f(L) = \frac{e^{-L/\lambda(s)} - e^{-L/\lambda(p)}}{1 - \lambda(p)/\lambda(s)} \tag{7}$$

where $\lambda(p)$ and $\lambda(s)$ are the nuclear interaction lengths for protons and pions or kaons, respectively, while for secondary protons:

$$f(L) = \frac{L}{\lambda(p)} \times e^{-L/\lambda(p)} \tag{8}$$

Table 14 lists the measured ratio of the particle yields for a target of length L divided by the yield of a 100 mm target for positive and negative secondaries. These ratios are also shown in figure 18, where they are compared to the predictions of the naive absorption model, for $\lambda(\pi) = 58.5$ cm, $\lambda(K) = 65.7$ cm, $\lambda(p) = 43.5$ cm. These values of the nuclear interaction lengths are derived from the absorption cross-sections of positive particles given in Reference [20]. When charge and momentum dependence of the absorption cross-sections [20, 21] are considered, ratios of target efficiencies around 1% lower than the ones drawn are predicted at low momenta, thus increasing the discrepancy between the naive absorption model and the experimental data. This points to cascade effects with tertiary particle production. These effects are well described in the available Monte Carlo generators of hadronic interactions [5, 6, 7].

5.3 Target shape dependence

The ratio of the pion yield from the T9-like target to the yield from the 100 mm plate target for the momentum scan performed at zero production angle and for the angular scans performed at 15 and 40 GeV/c are shown in Figures 19 and 20 respectively. At 15 and 40 GeV/c, where the flux dependence on the target thickness has been studied with plate targets, a direct comparison between the yield from the T9-like target and the 300 mm plate target is possible. The data show (see Figure 19) that in the forward direction these two targets give the same flux within the experimental error. Indeed, the secondary particle yields in the forward direction from targets of the same thickness along the beam axis must be independent of the target shape. As already noticed in the previous section, the observed yield relative to the 100 mm target is higher than the one expected on the basis of the naive absorption model, which neglects cascade effects with tertiary particle production. These effects are increasingly important at low momenta, while the model appears adequate at high momenta.

However, the geometry of the T9-like target should considerably reduce the absorption probability of particles produced at angles larger than a few milliradians, since particles can escape from the side of the target. Given the dimensions of the T9-like target, a gain in the target efficiency is expected at angles larger than 3 mrad as confirmed by the data of Figure 20.

A quantitative prediction can be obtained by a generalization of the naive absorption model. Indeed, following the arguments given in ref. [23], the efficiency of a target of any shape as a function of the production angle for secondary particles can be written as:

$$f(\theta, L) = \int_0^L \exp(-t(x)/\lambda_p) \exp(-t_{res}(x,\theta)/\lambda_s) \frac{dx}{\lambda_p} \tag{9}$$

where θ is the production angle, L the total length of the target; x is the longitudinal position along the target; $t(x)$ is the target thickness up to x and $t_{res}(x,\theta)$ is the residual target thickness that must be crossed by the secondary particle to escape from the target. The three terms of the integral represent respectively the probability that the primary proton does not interact up to x, the probability that the secondary particle is not reabsorbed and the probability that the primary proton does interact between x and $x + dx$.

The integration of the relation (9) in the case of the T9-like target geometry gives the full line shown in Figure 20. The dotted line in the figure has been obtained after rescaling the prediction of the naive absorption model to the production efficiency observed in the forward direction with the 300 mm standard target. The size of this rescaling is well predicted by the cascade models, mentioned in paragraph 5.2. Steps in the target efficiency as a function of the production angle are predicted, which reflect the discrete nature of the T9-like target structure. Data are in agreement with the prediction of the rescaled model. It is concluded that the naive absorption model, although inadequate to predict the absolute target efficiency, gives a satisfactory description of its angular dependence. Similar results are obtained for kaons and protons.

5.4 Inclusive invariant cross sections

Inclusive invariant cross sections on beryllium in the forward direction have been derived for secondary momenta at which particle yields from targets of at least two different thicknesses have been

measured.

The inclusive invariant particle production cross section is given by:

$$E \times \frac{d^3\sigma}{dp^3} = (100 \cdot Y) \cdot \frac{E}{p^3} \cdot \frac{A}{N_0 \cdot \rho \cdot \lambda_p \cdot f(L)} \tag{10}$$

where Y is the yield per incident proton per $sr(\Delta p/p\ \%)$; A, ρ, L are the atomic mass number, density and length of the target; N_0 is Avogadro's number; E and p the energy and momentum of secondaries, respectively. The target efficiency $f(L)$ has been estimated using formulae (7) or (8) from the naive absorption model. This model neglects the production of tertiaries, which our data show to be important especially at low momenta (see Section 5.2). This effect has been accounted for, in a model independent way, by estimating the invariant cross sections for various target lengths and then extrapolating the results to zero target thickness. This method has been cross-checked using the cascade model mentioned in paragraph 5.2 to estimate the amount of tertiares. The two methods give results on invariant cross-sections in good agreement within errors.

Table 15 and Figure 21 give the inclusive invariant cross section as a function of secondary momentum in the forward direction. Errors include the ones on the measured particle yields and systematic errors connected with the beam momentum estimate and with the method used for extrapolation at zero target length. The error on the invariant cross section is dominated by the uncertainty on the beam line acceptance.

This experiment extends to higher beam energies the studies on p-A interactions at 19.2 GeV/c by J.V.Allaby et al. [25], at 24 GeV/c by T.Eichten et al. [26] and at 100 GeV/c by D.S. Barton et al. [27] in a region where experimental data on invariant cross sections have not been previously available.

6 Conclusions

The present paper has reported on the measurement of the production ratios and particle yields in 450 GeV/c protons on beryllium interactions, for secondary particle momenta from 7 GeV/c up to 135 GeV/c, in the forward direction and with p_T values up to 600 MeV/c.

In particular, the measurement of the K/π ratio has been performed achieving an accuracy of about 3%. Charged particle yields $(\pi^{\pm}, K^{\pm}, p, \overline{p})$ have been measured with an experimental accuracy from 5% to 10% depending on beam momentum, which is comparable to the one obtained by previous experiments at higher momenta.

Additional results, obtained with targets of different thickness and shape, with respect to the standard plate target of 100 mm thickness have been also shown. Using the experimentally determined target thickness dependence, data have been extrapolated to zero thickness, giving a model independent determination of invariant cross sections in the forward direction. These results extend to higher energies the previous studies on proton nucleus interactions.

The presented measurements will be essential for the computation of flux and composition of present and future neutrino beams and of importance to check and tune the response of available Monte Carlo simulations of hadronic interactions.

Acknowledgements

We wish to thank all the staff and technical support at the SPS for the smooth operation of the accelerator during the NA56/SPY data taking period. We acknowledge G.R. Stevenson and the TIS/RP group for the calibration of primary beam monitors, S. Peraire and the SL/BT group for the preparation of the target box and N. Doble and the SL/BI group for help during the preparation and running of the experiment. We also acknowledge C. Baglin, A. Bussiere and J.P. Guillaud for their help with the wire chambers and A. De Min for his contribution to the early stages of this work.

We gratefully acknowledge the financial support of the different funding agencies: in particular the Australian Research Council (ARC) and the Department of Industry, Science and Tourism (DIST) (Australia), the Institut Interuniversitaire des Sciences Nucleaires (Belgium), the Academy of Finland (Finland), the Istituto Nazionale di Fisica Nucleare (Italy), the Schweizerischen Nationalfonds zur Förderung der Wissenschaftlichen Forschung (Switzerland) and the U.S. Department of Energy (U.S.A.).

References

[1] NA56/SPY Collaboration, G. Ambrosini *et al.* CERN-SPSLC/96-01, SPSLC/P294 (1996).

[2] G. Ambrosini *et al.*, Phys. Lett. B420 (1998), 225.
G. Ambrosini *et al.*, Phys. Lett. B425 (1998), 208.

[3] H.W. Atherton *et al.*, CERN 80-07, August 1980.

[4] A. J. Malensek, FERMILAB Report FN-341(1981).
J.R. Sanford, C.L. Wang, BNL/AGS Internal report JRS/CLW-1 (1967).

[5] R. Brun *et al.*, " GEANT: Detector Description and Simulation Tool", CERN Program Library Long Writeup W5013.

[6] A. Fassò *et al.*, Proc. of the Workshop on Simulating Radiation Environments, Santa Fe, USA, January 1993, LA-12835-C 1994 (p. 134).

[7] T.A. Gabriel *et al.*, ORNL/TM-11185
C. Zeitnitz, T.A. Gabriel, Nucl. Instr. Meth. A349 (1994) 106
CCC-610/CALOR95 Code Package, available from Oak Ridge National Laboratory, USA.

[8] G. Acquistapace *et al.*, CERN-ECP/95-14

[9] M. de Jong *et al.*, CHORUS Collaboration, CERN-PPE/93-131(1993)
E. Eskut *et al.*, Nucl. Instr. Meth. A401 (1997) 7.

[10] P. Astier *et al.*, NOMAD Collaboration, CERN-SPSLC/91-21(1990); CERN-SPSLC/91-48(1991); CERN-SPSLC/91-53(1991)
J. Altegoer *et al.*, Nucl. Instr. Meth. A404 (1998) 96.

[11] M. Bonesini *et al.*, CERN-SPSLC/95-37, SPSLC/I205 (1995).
J.J. Gomez Cadenas, J.A. Hernando, A. Bueno, Nucl. Inst. Meth. A378 (1996) 196.
J.J. Gomez Cadenas, J.A. Hernando, Nucl. Inst. Meth. A381 (1996) 223.
A.S. Ayan *et al.*, CERN-SPSC/97-5, SPSC/I213 (1997).
A. Rubbia *et al.*, CERN-SPSLC 96-58/P304, (1996).
M. Ambrosio *et al.*, NOE Collaboration, Nucl. Inst. Meth. A363 (1995), 604.
T. Ypsilantis, Nucl. Inst. Meth. A371 (1996), 330.
H. Shibuya *et al.*, CERN-SPSC/97-25, SPSC/I219 (1997) and LNGS-LOI 8/97 (1997).

[12] COSMOS Collaboration, 1995 Update Report on Fermilab E803/COSMOS.
MINOS Collaboration, Fermilab Report No. NuMI-L-63 (1995).
MINOS Collaboration, Fermilab Report No. NuMI-L-79 (1995).

[13] Y. Suzuki, Proc. XVII International Conference on Neutrino Physics and Astrophysics, Helsinki, Finland, June 13-19 (1996).

[14] G. Acquistapace *et al.*, CERN 98-02; INFN/AE-98/05

[15] K. Pretzl *et al.*, Invited talk at the International Symposium on Strangness and Quark Matter, Sept 1-5 1994, Krete (Greece). Published in the Conf. Prod. p. 230-244, ed. G. Vassiliadis, A.D. Panagiotou, S. Kumar, J. Madsen, World Scientific, 1995.

[16] P. Coet, N. Doble, CERN/SPS/86-23 (EBS).

[17] K. Bernier *et al.*, "Calibration of Secondary Emission Monitors of Absolute Proton Beam Intensity in the CERN SPS North Area", CERN 97-07 (1997).

[18] C. Bovet *et al.*, CERN 82-13, (1982).

[19] K.L. Brown, Ch. Iselin, "Decay Turtle", CERN 74-2.

[20] A.S. Carrol *et al.*, Phys. Lett. B80(1979) 319

[21] S.P. Denisov *et al.*, Nucl. Phys. B61(1973) 62
J.C. Allaby *et al.*, Sov. Journ. Nucl. Phys. 13(1971) 295.

[22] C. Caso *et al.*, Particle Data Group, Eur. Phys. Jour. C3 (1998) 1.

[23] M. Bonesini, S. Ragazzi and T. Tabarelli de Fatis, Nucl. Instr. Meth. A378 (1996) 349.

[24] N. Doble *et al.*, NA31 Internal note 83 (1990).

[25] J.V.Allaby *et al.*, CERN 70-12.

[26] T. Eichten *et al.*, Nucl. Phys. B44(1972) 333.

[27] D. S. Barton *et al.*, Phys. Rev. D27(1983) 2580.

p/z (GeV/c)	Target	Angles (mrad)
+135	100,200,300 mm,T9	0
+67.5	100 mm	0
+40	100 mm	$-15, \pm 11.25, \pm 5.625, +3.75, +1.875, 0$
	T9	$-15, +5.625, 0$
	200,300 mm	0
+30	100 mm,T9	0
+20	100 mm,T9	0
+15	100 mm	$+30, +22.5, \pm 15, \pm 10, +5, 0$
	T9	$-15, +5, 0$
	200,300 mm	0
+10	100,200,300 mm,T9	0
+7	100 mm,T9	0
-67.5	100 mm,T9	0
-40	100 mm	$-15, -11.25, -5.625, \pm 3.75, \pm 1.875, 0$
	200,300 mm, T9	0
-15	100 mm	$-15, -5, 0$
	300 mm,T9	0
-10	100 mm	0
-7	100 mm,T9	0

Table 1: Summary of data samples collected in the NA56/SPY experiment. p/z is the secondary particle rigidity.

p (GeV/c)		$\mathcal{A}_A$ (μsr %$\Delta p/p$)	$\mathcal{T}_B$	$\mathcal{T}_B^{data}/\mathcal{T}_B^{Turtle}$
	$\pi^{\pm}$	2.99×10^{-3}	0.898	–
135	p	2.96×10^{-3}	0.863	0.98
	$\pi^{\pm}$	2.96×10^{-3}	0.898	–
67.5	p	2.93×10^{-3}	0.863	*0.98*
	$\pi^{\pm}$	15.10×10^{-3}	0.895	–
40	p	14.85×10^{-3}	0.861	0.98
	$\pi^{\pm}$	14.99×10^{-3}	0.879	–
30	p	14.74×10^{-3}	0.844	*0.96*
	$\pi^{\pm}$	15.08×10^{-3}	0.856	–
20	p	14.79×10^{-3}	0.828	*0.94*
	$\pi^{\pm}$	15.03×10^{-3}	0.698	–
15	p	14.79×10^{-3}	0.674	0.92
	$\pi^{\pm}$	14.07×10^{-3}	–	–
10	p	13.76×10^{-3}	–	–
	$\pi^{\pm}$	11.28×10^{-3}	–	–
7	p	11.16×10^{-3}	–	–

Table 2: Spectrometer acceptances for the SPY setup. The final acceptances $\mathcal{A}$ were calculated from the acceptance $\mathcal{A}_A$ at B1 (column 2) and the computed transmission downstream of B1 (column 3) rescaled by the discrepancy between the proton transmission predicted by the TURTLE simulation and observed in the data (column 4). In column 4, values in *italic* were interpolated from the available measurements. For 7 and 10 GeV/c numbers are quoted for the "run A_L" configuration, up to TOF3 (10 GeV/c) and B1 (7 GeV/c).

nominal p/z (GeV/c)	measured p/z (GeV/c)	
± 7	7.167 ± 0.002	-6.973 ± 0.002
± 10	10.112 ± 0.002	-10.004 ± 0.003
± 15	15.178 ± 0.005	-15.065 ± 0.005
± 20	20.14 ± 0.02	-
± 30	30.16 ± 0.04	-
± 40	40.30 ± 0.10	-40.40 ± 0.15
± 67.5	67.5 ± 0.5	-67.5 ± 0.5
± 135.0	135.0 ± 0.5	-

Table 3: Nominal and measured secondary particle rigidity (p/z) for the various groups of runs used in the data analysis

p/z (GeV/c)	π	K	p
	(incident protons $\cdot$ sr $\cdot$ $(\Delta p/p\ \%))^{-1}$		
+7.	$0.317 \pm 0.003 \pm 0.031$	$0.022 \pm 0.001 \pm 0.002$	$0.0130 \pm 0.0001 \pm 0.0014$
	$(0.336 \pm 0.003 \pm 0.033)$		$(0.0153 \pm 0.0001 \pm 0.0015)$
+10.	$0.493 \pm 0.005 \pm 0.040$	$0.037 \pm 0.001 \pm 0.003$	$0.0220 \pm 0.0001 \pm 0.0020$
	$(0.515 \pm 0.005 \pm 0.043)$		$(0.0248 \pm 0.0001 \pm 0.0021)$
+15.	$0.859 \pm 0.003 \pm 0.086$	$0.072 \pm 0.002 \pm 0.007$	$0.0453 \pm 0.0005 \pm 0.0047$
	$(0.891 \pm 0.003 \pm 0.089)$		$(0.0501 \pm 0.0006 \pm 0.0050)$
+20.	$1.271 \pm 0.004 \pm 0.102$	$0.122 \pm 0.002 \pm 0.010$	$0.0819 \pm 0.0008 \pm 0.0069$
	$(1.314 \pm 0.004 \pm 0.105)$		$(0.0898 \pm 0.0009 \pm 0.0072)$
+30.	$2.15 \pm 0.01 \pm 0.13$	$0.228 \pm 0.003 \pm 0.014$	$0.194 \pm 0.002 \pm 0.013$
	$(2.20 \pm 0.01 \pm 0.14)$		$(0.208 \pm 0.002 \pm 0.013)$
+40.	$3.01 \pm 0.01 \pm 0.15$	$0.330 \pm 0.003 \pm 0.017$	$0.357 \pm 0.002 \pm 0.019$
	$(3.07 \pm 0.01 \pm 0.15)$		$(0.375 \pm 0.003 \pm 0.019)$
+67.5	$5.30 \pm 0.02 \pm 0.35$	$0.560 \pm 0.006 \pm 0.037$	$1.206 \pm 0.009 \pm 0.080$
	$(5.37 \pm 0.02 \pm 0.36)$		$(1.232 \pm 0.009 \pm 0.082)$
+135.	$11.89 \pm 0.05 \pm 0.79$	$0.960 \pm 0.011 \pm 0.064$	$7.64 \pm 0.04 \pm 0.51$
	$(12.03 \pm 0.05 \pm 0.80)$		$(7.80 \pm 0.04 \pm 0.52)$
-7.	$0.254 \pm 0.006 \pm 0.026$	$0.016 \pm 0.001 \pm 0.002$	$0.0038 \pm 0.0001 \pm 0.0004$
	$(0.278 \pm 0.008 \pm 0.027)$		$(0.0041 \pm 0.0001 \pm 0.0004)$
-10.	$0.366 \pm 0.005 \pm 0.029$	$0.026 \pm 0.002 \pm 0.002$	$0.0078 \pm 0.0001 \pm 0.0006$
	$(0.401 \pm 0.006 \pm 0.030)$		$(0.0083 \pm 0.0001 \pm 0.0006)$
-15.	$0.701 \pm 0.002 \pm 0.071$	$0.053 \pm 0.001 \pm 0.005$	$0.0195 \pm 0.0003 \pm 0.0019$
	$(0.750 \pm 0.003 \pm 0.075)$		$(0.0203 \pm 0.0003 \pm 0.0019)$
-40.	$2.40 \pm 0.01 \pm 0.12$	$0.208 \pm 0.004 \pm 0.011$	$0.0875 \pm 0.0014 \pm 0.0045$
	$(2.46 \pm 0.01 \pm 0.12)$		$(0.0904 \pm 0.0015 \pm 0.0046)$
-67.5	$3.08 \pm 0.01 \pm 0.21$	$0.263 \pm 0.005 \pm 0.017$	$0.1103 \pm 0.0019 \pm 0.0074$
	$(3.13 \pm 0.01 \pm 0.21)$		$(0.1145 \pm 0.0020 \pm 0.0076)$

Table 4: Particle yields from the 100 mm Be target in the forward direction as a function of the particle rigidity p/z. The first error is statistical; the second is the total systematic error. Values in parentheses are not corrected for the pion, proton or antiproton flux coming from strange particle decays.

p (GeV/c)	K^+/π^+	K^-/π^-
7	$0.0691 \pm 0.0029 \pm 0.0012$	$0.0635 \pm 0.0046 \pm 0.0052$
	$(0.0656 \pm 0.0028 \pm 0.0008)$	$(0.0580 \pm 0.0042 \pm 0.0046)$
10	$0.0741 \pm 0.0020 \pm 0.0013$	$0.0697 \pm 0.0033 \pm 0.0018$
	$(0.0709 \pm 0.0019 \pm 0.0009)$	$(0.0634 \pm 0.0030 \pm 0.0008)$
15	$0.0832 \pm 0.0024 \pm 0.0014$	$0.0751 \pm 0.0020 \pm 0.0017$
	$(0.0803 \pm 0.0023 \pm 0.0011)$	$(0.0702 \pm 0.0019 \pm 0.0009)$
20	$0.0965 \pm 0.0018 \pm 0.0014$	
	$(0.0933 \pm 0.0017 \pm 0.0011)$	
30	$0.1060 \pm 0.0016 \pm 0.0011$	
	$(0.1036 \pm 0.0016 \pm 0.0009)$	
40	$0.1096 \pm 0.0010 \pm 0.0013$	$0.0868 \pm 0.0016 \pm 0.0011$
	$(0.1075 \pm 0.0010 \pm 0.0011)$	$(0.0846 \pm 0.0016 \pm 0.0009)$
67.5	$0.1057 \pm 0.0012 \pm 0.0013$	$0.0853 \pm 0.0017 \pm 0.0010$
	$(0.1044 \pm 0.0012 \pm 0.0012)$	$(0.0841 \pm 0.0017 \pm 0.0009)$
135	$0.0807 \pm 0.0010 \pm 0.0010$	
	$(0.0798 \pm 0.0010 \pm 0.0010)$	

Table 5: K/π production ratios with the 100 mm Be target in the forward direction as a function of secondary particle momentum. The first error is statistical; the second includes all the systematic uncertainties added in quadrature (see text for details). Values in parentheses are not corrected for the pion flux coming from strange particle decays.

p (GeV/c)	K^+/p	$K^-/\overline{p}$
7	$1.685 \pm 0.069 \pm 0.099$	$4.31 \pm 0.30 \pm 0.37$
	$(1.442 \pm 0.059 \pm 0.022)$	$(3.96 \pm 0.28 \pm 0.32)$
10	$1.657 \pm 0.042 \pm 0.078$	$3.259 \pm 0.147 \pm 0.085$
	$(1.470 \pm 0.038 \pm 0.023)$	$(3.070 \pm 0.139 \pm 0.047)$
15	$1.582 \pm 0.041 \pm 0.060$	$2.715 \pm 0.059 \pm 0.058$
	$(1.427 \pm 0.037 \pm 0.025)$	$(2.614 \pm 0.056 \pm 0.046)$
20	$1.497 \pm 0.022 \pm 0.051$	
	$(1.365 \pm 0.020 \pm 0.023)$	
30	$1.177 \pm 0.012 \pm 0.031$	
	$(1.096 \pm 0.011 \pm 0.017)$	
40	$0.924 \pm 0.006 \pm 0.020$	$2.377 \pm 0.017 \pm 0.045$
	$(0.878 \pm 0.005 \pm 0.014)$	$(2.300 \pm 0.016 \pm 0.038)$
67.5	$0.464 \pm 0.004 \pm 0.008$	$2.382 \pm 0.018 \pm 0.046$
	$(0.455 \pm 0.004 \pm 0.007)$	$(2.296 \pm 0.017 \pm 0.038)$
135	$0.126 \pm 0.001 \pm 0.002$	
	$(0.123 \pm 0.001 \pm 0.002)$	

Table 6: K/p production ratios with the 100 mm Be target in the forward direction as a function of secondary particle momentum. The first error is statistical; the second includes all the systematic uncertainties added in quadrature (see text for details). Values in parentheses are not corrected for the proton or antiproton flux coming from strange particle decays.

p (GeV/c)	p/π^+	$\overline{p}/\pi^-$
7	$0.0410 \pm 0.0004 \pm 0.0021$	$0.0148 \pm 0.0005 \pm 0.0006$
	$(0.0455 \pm 0.0005 \pm 0.0006)$	$(0.0147 \pm 0.0005 \pm 0.0002)$
10	$0.0447 \pm 0.0003 \pm 0.0019$	$0.0214 \pm 0.0004 \pm 0.0007$
	$(0.0482 \pm 0.0004 \pm 0.0007)$	$(0.0206 \pm 0.0004 \pm 0.0003)$
15	$0.0526 \pm 0.0006 \pm 0.0018$	$0.0277 \pm 0.0004 \pm 0.0006$
	$(0.0563 \pm 0.0007 \pm 0.0006)$	$(0.0269 \pm 0.0004 \pm 0.0003)$
20	$0.0644 \pm 0.0007 \pm 0.0020$	
	$(0.0683 \pm 0.0007 \pm 0.0008)$	
30	$0.0901 \pm 0.0010 \pm 0.0021$	
	$(0.0946 \pm 0.0010 \pm 0.0011)$	
40	$0.1188 \pm 0.0009 \pm 0.0023$	$0.0366 \pm 0.0006 \pm 0.0006$
	$(0.1224 \pm 0.0009 \pm 0.0015)$	$(0.0368 \pm 0.0006 \pm 0.0004)$
67.5	$0.2275 \pm 0.0019 \pm 0.0031$	$0.0359 \pm 0.0006 \pm 0.0006$
	$(0.2296 \pm 0.0019 \pm 0.0027)$	$(0.0367 \pm 0.0007 \pm 0.0004)$
135	$0.6423 \pm 0.0042 \pm 0.0087$	
	$(0.6482 \pm 0.0042 \pm 0.0077)$	

Table 7: p/π production ratios with the 100 mm Be target in the forward direction as a function of secondary particle momentum. The first error is statistical; the second includes all the systematic uncertainties added in quadrature (see text for details). Values in parentheses are not corrected for the proton, antiproton or pion flux coming from strange particle decays.

p_T (MeV/c)	$p/z = +15$ GeV/c	$p/z = -15$ GeV/c	$p/z = +40$ GeV/c	$p/z = -40$ GeV/c
0.0	$0.859 \pm 0.003 \pm 0.015$	$0.701 \pm 0.002 \pm 0.012$	$3.007 \pm 0.008 \pm 0.048$	$2.396 \pm 0.008 \pm 0.034$
	$(0.891 \pm 0.003 \pm 0.013)$	$(0.750 \pm 0.003 \pm 0.011)$	$(3.068 \pm 0.008 \pm 0.046)$	$(2.458 \pm 0.009 \pm 0.037)$
75.0	$0.905 \pm 0.003 \pm 0.016$	$0.709 \pm 0.003 \pm 0.012$	$3.122 \pm 0.011 \pm 0.048$	$2.430 \pm 0.008 \pm 0.039$
	$(0.939 \pm 0.003 \pm 0.014)$	$(0.760 \pm 0.003 \pm 0.011)$	$(3.170 \pm 0.011 \pm 0.048)$	$(2.480 \pm 0.006 \pm 0.037)$
150.0	$0.818 \pm 0.002 \pm 0.014$	-	$3.303 \pm 0.011 \pm 0.051$	$2.367 \pm 0.006 \pm 0.037$
	$(0.845 \pm 0.002 \pm 0.013)$	-	$(3.351 \pm 0.012 \pm 0.050)$	$(2.409 \pm 0.008 \pm 0.036)$
225.0	$0.620 \pm 0.001 \pm 0.011$	$0.486 \pm 0.002 \pm 0.008$	$2.851 \pm 0.007 \pm 0.045$	$2.007 \pm 0.007 \pm 0.031$
	$(0.641 \pm 0.002 \pm 0.010)$	$(0.516 \pm 0.002 \pm 0.008)$	$(2.893 \pm 0.007 \pm 0.044)$	$(2.042 \pm 0.007 \pm 0.031)$
337.5	$0.345 \pm 0.001 \pm 0.005$	-	-	-
	$(0.357 \pm 0.001 \pm 0.005)$	-	-	-
450.0	$0.187 \pm 0.001 \pm 0.003$	-	$1.053 \pm 0.002 \pm 0.017$	$0.784 \pm 0.003 \pm 0.012$
	$(0.193 \pm 0.001 \pm 0.003)$	-	$(1.071 \pm 0.002 \pm 0.017)$	$(0.797 \pm 0.003 \pm 0.012)$
600.0	-	-	$0.420 \pm 0.002 \pm 0.007$	$0.364 \pm 0.001 \pm 0.006$
	-	-	$(0.426 \pm 0.002 \pm 0.006)$	$(0.370 \pm 0.001 \pm 0.006)$

Table 8: Pion yields per (incident protons · sr · ($\Delta p/p$ %)) with the 100 mm Be target as a function of the transverse momentum. Values in parentheses are not corrected for the pion flux coming from strange particle decays. The first error is statistical, the second gives the point to point systematic uncertainty. Common systematic errors are not included and amount to $10\%(5\%)$ at 15 (40) GeV/c (see text).

p_T (MeV/c)	$p/z = +15$ GeV/c	$p/z = -15$ GeV/c	$p/z = +40$ GeV/c	$p/z = -40$ GeV/c
0.0	$0.0715 \pm 0.0021 \pm 0.0011$	$0.0526 \pm 0.0014 \pm 0.0008$	$0.3296 \pm 0.0030 \pm 0.0050$	$0.2081 \pm 0.0038 \pm 0.0031$
75.0	$0.0729 \pm 0.0021 \pm 0.0011$	$0.0496 \pm 0.0013 \pm 0.0007$	$0.3234 \pm 0.0041 \pm 0.0049$	$0.2063 \pm 0.0026 \pm 0.0031$
150.0	$0.0663 \pm 0.0014 \pm 0.0010$	-	$0.3029 \pm 0.0039 \pm 0.0046$	$0.1888 \pm 0.0024 \pm 0.0029$
225.0	$0.0543 \pm 0.0009 \pm 0.0008$	$0.0382 \pm 0.0011 \pm 0.0006$	$0.2634 \pm 0.0024 \pm 0.0040$	$0.1598 \pm 0.0028 \pm 0.0024$
337.5	$0.0405 \pm 0.0013 \pm 0.0006$	-	-	-
450.0	$0.0253 \pm 0.0009 \pm 0.0004$	-	$0.1394 \pm 0.0010 \pm 0.0021$	$0.0835 \pm 0.0012 \pm 0.0012$
600.0	-	-	$0.0712 \pm 0.0008 \pm 0.0011$	$0.0467 \pm 0.0007 \pm 0.0007$

Table 9: Kaon yields per (incident protons · sr · ($\Delta p/p$ %)) with the 100 mm Be target as a function of the transverse momentum. The first error is statistical, the second gives the point to point systematic uncertainty. Common systematic errors are not included and amount to $10\%(5\%)$ at 15 (40) GeV/c (see text).

p_T (MeV/c)	$p/z = +15$ GeV/c	$p/z = -15$ GeV/c	$p/z = +40$ GeV/c	$p/z = -40$ GeV/c
0.0	$0.0453 \pm 0.0005 \pm 0.0015$	$0.0195 \pm 0.0003 \pm 0.0003$	$0.3569 \pm 0.0024 \pm 0.0074$	$0.0875 \pm 0.0014 \pm 0.0015$
	$(0.0501 \pm 0.0006 \pm 0.0008)$	$(0.0203 \pm 0.0003 \pm 0.0003)$	$(0.3753 \pm 0.0025 \pm 0.0056)$	$(0.0904 \pm 0.0015 \pm 0.0013)$
75.0	$0.0439 \pm 0.0005 \pm 0.0019$	$0.0194 \pm 0.0003 \pm 0.0003$	$0.3536 \pm 0.0033 \pm 0.0071$	$0.0877 \pm 0.0010 \pm 0.0015$
	$(0.0503 \pm 0.0006 \pm 0.0008)$	$(0.0202 \pm 0.0003 \pm 0.0003)$	$(0.3714 \pm 0.0035 \pm 0.0056)$	$(0.0906 \pm 0.0011 \pm 0.0013)$
150.0	$0.0423 \pm 0.0003 \pm 0.0014$	-	$0.3344 \pm 0.0033 \pm 0.0067$	$0.0821 \pm 0.0010 \pm 0.0014$
	$(0.0467 \pm 0.0003 \pm 0.0007)$	-	$(0.3509 \pm 0.0034 \pm 0.0053)$	$(0.0847 \pm 0.0010 \pm 0.0013)$
225.0	$0.0385 \pm 0.0002 \pm 0.0015$	$0.0155 \pm 0.0003 \pm 0.0003$	$0.3095 \pm 0.0021 \pm 0.0061$	$0.0730 \pm 0.0012 \pm 0.0012$
	$(0.0427 \pm 0.0002 \pm 0.0006)$	$(0.0161 \pm 0.0003 \pm 0.0003)$	$(0.3231 \pm 0.0021 \pm 0.0050)$	$(0.0751 \pm 0.0012 \pm 0.0011)$
337.5	$0.0303 \pm 0.0003 \pm 0.0013$	-	-	-
	$(0.0345 \pm 0.0003 \pm 0.0005)$	-	-	-
450.0	$0.0225 \pm 0.0002 \pm 0.0013$	-	$0.1866 \pm 0.0008 \pm 0.0041$	$0.0447 \pm 0.0006 \pm 0.0008$
	$(0.0261 \pm 0.0002 \pm 0.0004)$	-	$(0.1961 \pm 0.0008 \pm 0.0030)$	$(0.0461 \pm 0.0006 \pm 0.0007)$
600.0	-	-	$0.1053 \pm 0.0007 \pm 0.0021$	$0.0277 \pm 0.0003 \pm 0.0005$
	-	-	$(0.1094 \pm 0.0007 \pm 0.0016)$	$(0.0285 \pm 0.0004 \pm 0.0004)$

Table 10: Proton yields per (incident protons · sr · ($\Delta p/p$ %)) with the 100 mm Be target as a function of the transverse momentum. Values in parentheses are not corrected for the proton/antiproton flux coming from strange particle decays. The first error is statistical, the second gives the point to point systematic uncertainty. Common systematic errors are not included and amount to $10\%(5\%)$ at 15 (40) GeV/c (see text).

p_T (MeV/c)	$p/z = +15$ GeV/c	$p/z = -15$ GeV/c	$p/z = +40$ GeV/c	$p/z = -40$ GeV/c
0.0	$0.0832 \pm 0.0024 \pm 0.0009$	$0.0751 \pm 0.0020 \pm 0.0014$	$0.1096 \pm 0.0010 \pm 0.0007$	$0.0868 \pm 0.0016 \pm 0.0006$
	(0.0803 ± 0.0023)	(0.0702 ± 0.0019)	(0.1075 ± 0.0010)	(0.0846 ± 0.0016)
75.0	$0.0805 \pm 0.0023 \pm 0.0009$	$0.0700 \pm 0.0020 \pm 0.0013$	$0.1036 \pm 0.0014 \pm 0.0005$	$0.0849 \pm 0.0011 \pm 0.0004$
	(0.0776 ± 0.0022)	(0.0653 ± 0.0018)	(0.1020 ± 0.0014)	(0.0833 ± 0.0011)
150.0	$0.0810 \pm 0.0017 \pm 0.0008$	-	$0.0917 \pm 0.0012 \pm 0.0004$	$0.0796 \pm 0.0010 \pm 0.0004$
	(0.0785 ± 0.0016)	-	(0.0905 ± 0.0012)	(0.0783 ± 0.0010)
225.0	$0.0876 \pm 0.0014 \pm 0.0009$	$0.0786 \pm 0.0022 \pm 0.0012$	$0.0924 \pm 0.0008 \pm 0.0004$	$0.0796 \pm 0.0014 \pm 0.0004$
	(0.0849 ± 0.0014)	(0.0740 ± 0.0021)	(0.0912 ± 0.0008)	(0.0783 ± 0.0014)
337.5	$0.1176 \pm 0.0035 \pm 0.0011$	-	-	-
	(0.1139 ± 0.0034)	-	-	-
450.0	$0.1360 \pm 0.0044 \pm 0.0012$	-	$0.1324 \pm 0.0009 \pm 0.0005$	$0.1065 \pm 0.0016 \pm 0.0005$
	(0.1318 ± 0.0043)	-	(0.1303 ± 0.0009)	(0.1049 ± 0.0016)
600.0	-	-	$0.1693 \pm 0.0020 \pm 0.0006$	$0.1286 \pm 0.0018 \pm 0.0005$
	-	-	(0.1671 ± 0.0020)	(0.1264 ± 0.0018)

Table 11: K/π production ratios with the 100 mm Be target as a function of the transverse momentum. Values in parentheses are not corrected for the pion flux coming from strange particle decays. The first error is statistical, the second gives the systematic uncertainty due to the correction for strange particle decays. Common systematic errors are not included and amount to 1.3% at 15 GeV/c and to 1.1% at 40 GeV/c (see text).

p_T (MeV/c)	$p/z = +15$ GeV/c	$p/z = -15$ GeV/c	$p/z = +40$ GeV/c	$p/z = -40$ GeV/c
0.0	$1.582 \pm 0.041 \pm 0.053$	$2.715 \pm 0.059 \pm 0.033$	$0.924 \pm 0.006 \pm 0.014$	$2.377 \pm 0.016 \pm 0.023$
	(1.427 ± 0.037)	(2.614 ± 0.056)	(0.878 ± 0.005)	(2.300 ± 0.016)
75.0	$1.662 \pm 0.044 \pm 0.077$	$2.545 \pm 0.058 \pm 0.031$	$0.915 \pm 0.008 \pm 0.013$	$2.352 \pm 0.012 \pm 0.022$
	(1.448 ± 0.038)	(2.451 ± 0.055)	(0.871 ± 0.007)	(2.279 ± 0.011)
150.0	$1.567 \pm 0.029 \pm 0.050$	-	$0.906 \pm 0.008 \pm 0.013$	$2.299 \pm 0.011 \pm 0.021$
	(1.421 ± 0.026)	-	(0.863 ± 0.007)	(2.228 ± 0.011)
225.0	$1.418 \pm 0.022 \pm 0.053$	$2.448 \pm 0.057 \pm 0.029$	$0.850 \pm 0.005 \pm 0.011$	$2.188 \pm 0.015 \pm 0.018$
	(1.275 ± 0.020)	(2.358 ± 0.055)	(0.815 ± 0.005)	(2.128 ± 0.015)
337.5	$1.339 \pm 0.038 \pm 0.061$	-	-	-
	(1.176 ± 0.034)	-	-	-
450.0	$1.124 \pm 0.036 \pm 0.068$	-	$0.748 \pm 0.004 \pm 0.012$	$1.870 \pm 0.014 \pm 0.019$
	(0.971 ± 0.031)	-	(0.713 ± 0.004)	(1.813 ± 0.013)
600.0	-	-	$0.676 \pm 0.006 \pm 0.010$	$1.687 \pm 0.013 \pm 0.016$
	-	-	(0.651 ± 0.006)	(1.647 ± 0.013)

Table 12: K/p production ratios with the 100 mm Be target as a function of the transverse momentum. Values in parentheses are not corrected for the proton/antiproton flux coming from strange particle decays. The first error is statistical, the second gives the systematic uncertainty due to the correction for strange particle decays. Common systematic errors are not included and amount to 1.7% at 15 GeV/c and to 1.5% at 40 GeV/c (see text).

p_T (MeV/c)	$p/z = +15$ GeV/c	$p/z = -15$ GeV/c	$p/z = +40$ GeV/c	$p/z = -40$ GeV/c
0.0	$0.0526 \pm 0.0006 \pm 0.0017$	$0.0277 \pm 0.0004 \pm 0.0006$	$0.1188 \pm 0.0009 \pm 0.0018$	$0.0366 \pm 0.0006 \pm 0.0004$
	(0.0563 ± 0.0007)	(0.0269 ± 0.0004)	(0.1224 ± 0.0009)	(0.0368 ± 0.0006)
75.0	$0.0484 \pm 0.0006 \pm 0.0020$	$0.0275 \pm 0.0004 \pm 0.0005$	$0.1132 \pm 0.0011 \pm 0.0016$	$0.0362 \pm 0.0004 \pm 0.0004$
	(0.0536 ± 0.0006)	(0.0266 ± 0.0004)	(0.1172 ± 0.0012)	(0.0366 ± 0.0004)
150.0	$0.0518 \pm 0.0004 \pm 0.0016$	-	$0.1012 \pm 0.0010 \pm 0.0014$	$0.0346 \pm 0.0004 \pm 0.0003$
	(0.0553 ± 0.0004)	-	(0.1047 ± 0.0011)	(0.0352 ± 0.0004)
225.0	$0.0619 \pm 0.0004 \pm 0.0022$	$0.0322 \pm 0.0005 \pm 0.0006$	$0.1086 \pm 0.0008 \pm 0.0014$	$0.0364 \pm 0.0006 \pm 0.0003$
	(0.0667 ± 0.0004)	(0.0314 ± 0.0005)	(0.1117 ± 0.0008)	(0.0368 ± 0.0006)
337.5	$0.0878 \pm 0.0008 \pm 0.0036$	-	-	-
	(0.0968 ± 0.0009)	-	-	-
450.0	$0.1211 \pm 0.0010 \pm 0.0065$	-	$0.1772 \pm 0.0008 \pm 0.0028$	$0.0569 \pm 0.0008 \pm 0.0006$
	(0.1359 ± 0.0012)	-	(0.1831 ± 0.0009)	(0.0579 ± 0.0008)
600.0	-	-	$0.2505 \pm 0.0019 \pm 0.0036$	$0.0763 \pm 0.0010 \pm 0.0008$
	-	-	(0.2569 ± 0.0020)	(0.0767 ± 0.0009)

Table 13: p/π production ratios with the 100 mm Be target as a function of the transverse momentum. Values in parentheses are not corrected for the pion or proton/antiproton flux coming from strange particle decays. The first error is statistical, the second gives the systematic uncertainty due to the correction for strange particle decays. Common systematic errors are not included and amount to 1.1% (see text).

	$p/z = +10$ GeV/c	$p/z = +15$ GeV/c	$p/z = +40$ GeV/c	$p/z = -40$ GeV/c
π	-	$1.733 \pm .049$	$1.788 \pm .057$	$1.687 \pm .056$
	$(2.378 \pm .069)$	$(2.244 \pm .064)$	$(2.321 \pm .074)$	$(2.198 \pm .073)$
K	$1.911 \pm .097$	$1.895 \pm .083$	$1.714 \pm .066$	$1.681 \pm .079$
	$(2.651 \pm .118)$	$(2.453 \pm .106)$	$(2.262 \pm .087)$	$(2.248 \pm .106)$
p	$2.004 \pm .075$	$1.909 \pm .060$	$1.775 \pm .058$	$1.625 \pm .064$
	$(2.790 \pm .103)$	$(2.545 \pm .080)$	$(2.421 \pm .076)$	$(2.061 \pm .084)$

Table 14: Yields from a plate Be target of 200 mm (300 mm) relative to the 100 mm one, in the forward direction. The quoted error includes statistical and systematic uncertainties.

p/z (GeV/c)	π (mb/GeV^2)	K (mb/GeV^2)	p (mb/GeV^2)
+7.	532.6 ± 55.7	29.9 ± 3.4	21.0 ± 3.0
+10.	433.4 ± 38.3	30.2 ± 3.1	16.8 ± 1.6
+15.	347.9 ± 35.2	27.1 ± 3.0	16.7 ± 1.9
+20.	293.0 ± 24.8	27.0 ± 2.5	18.0 ± 1.6
+30.	222.0 ± 14.9	22.2 ± 1.6	18.9 ± 1.5
+40.	169.7 ± 9.7	18.4 ± 1.1	19.2 ± 1.2
+67.5	111.1 ± 7.0	11.7 ± 0.9	24.4 ± 1.8
+135.	64.0 ± 4.6	5.0 ± 0.4	40.6 ± 3.0
-7.	490.0 ± 55.6	26.6 ± 4.7	6.1 ± 0.9
-15.	289.2 ± 30.3	21.4 ± 2.2	8.5 ± 0.9
-40.	137.8 ± 7.8	11.5 ± 0.8	5.2 ± 0.3
-67.5	64.5 ± 4.7	5.5 ± 0.4	2.4 ± 0.2

Table 15: Inclusive invariant cross section for p-Be interactions at 450 GeV/c as a function of the particle rigidity p/z, in the forward direction. Quoted errors include statistical and systematics errors.

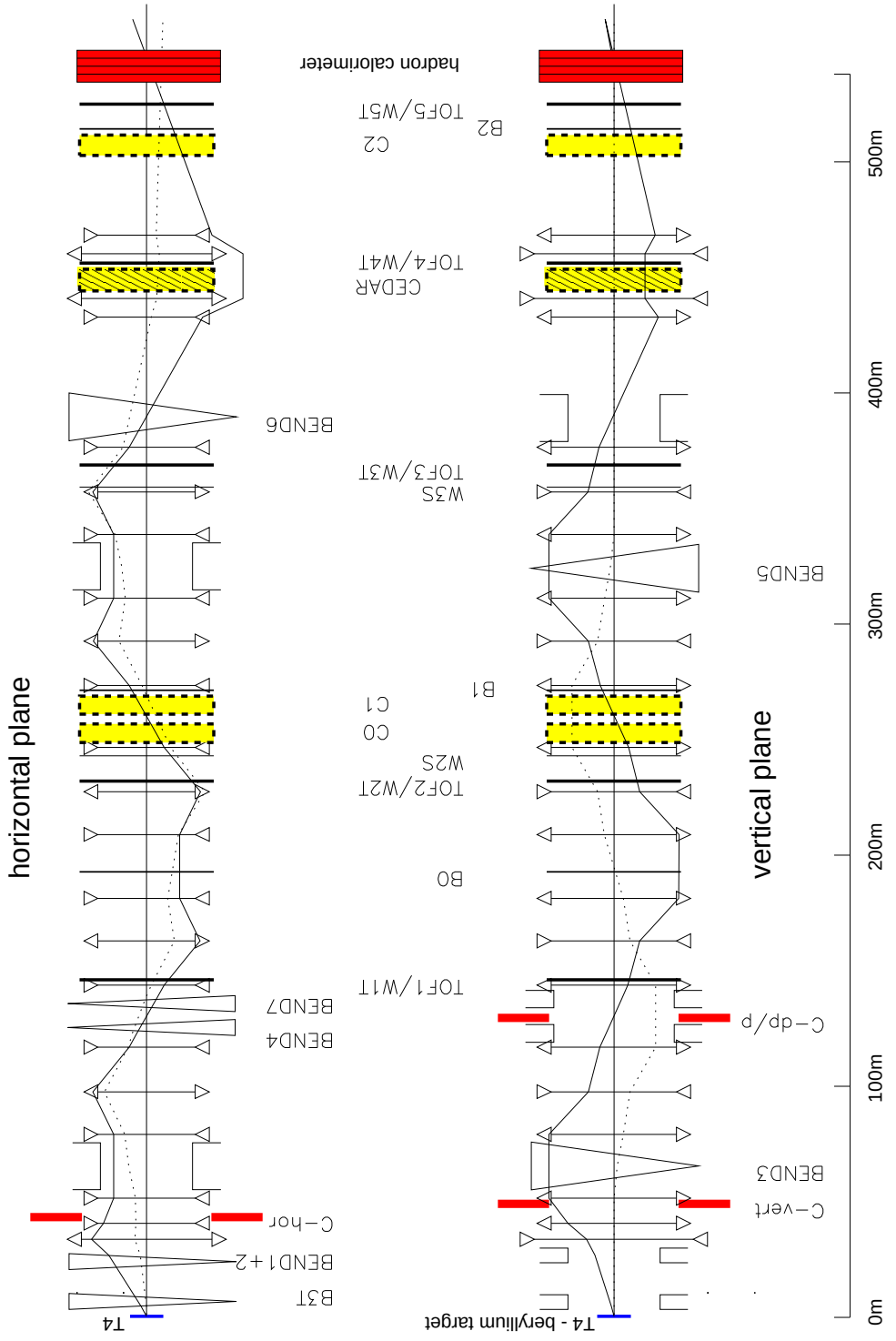

Figure 1: The NA56/SPY experimental set-up: elements of the beam optics in the horizontal and vertical bending planes are also shown. Not to scale, the solid line indicates the excursion of a particle which starts with an angular offset at T4 (1 mrad) and the dotted line shows the trajectories of on-axis particles with a momentum different from the nominal one ($\Delta p/p \sim 1\%$).

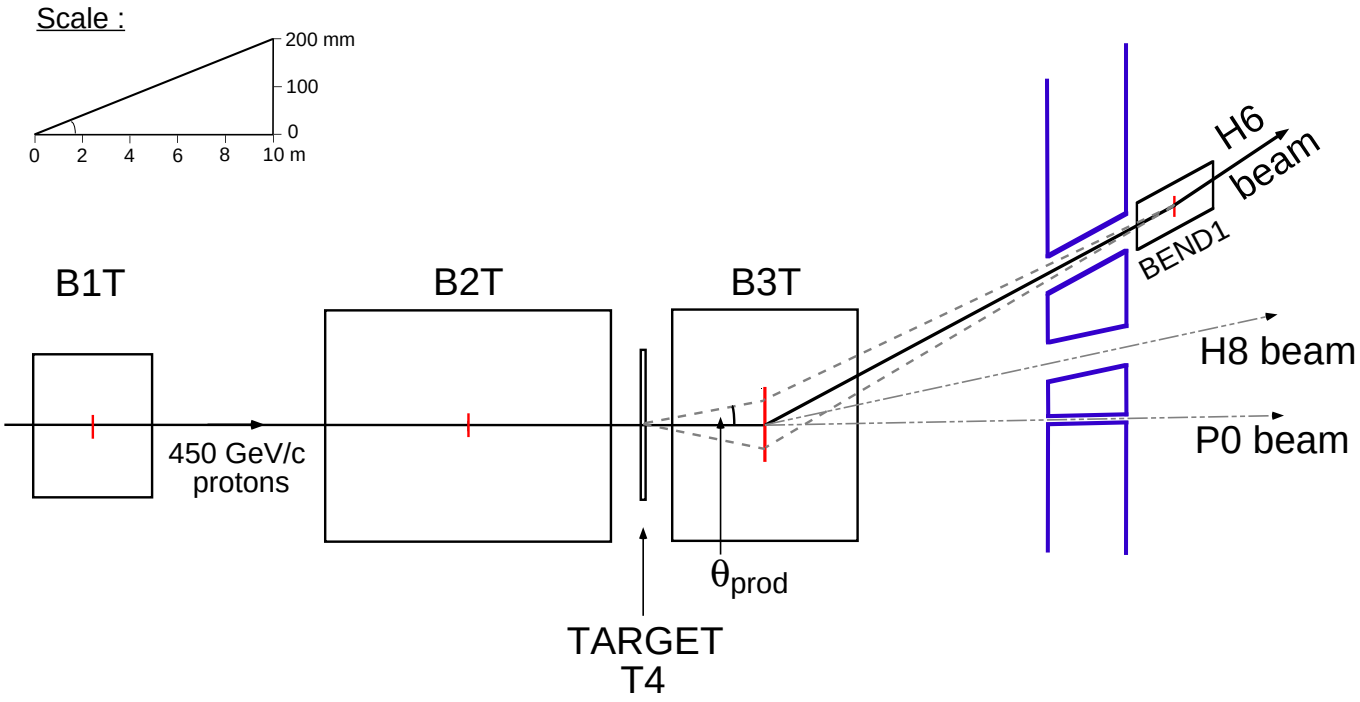

Figure 2: Plan of target station T4.

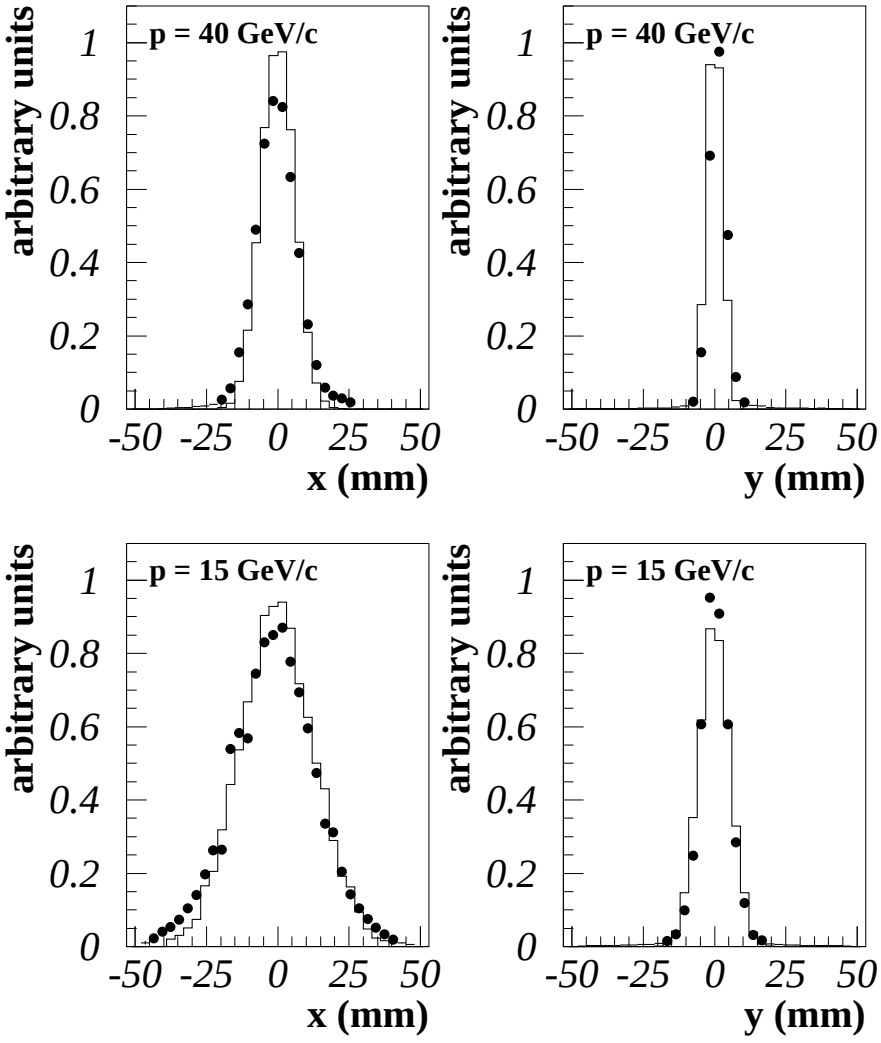

Figure 3: Beam profiles at TOF2 for 40 and 15 GeV/c protons: data (full dots) and TURTLE Monte Carlo (solid line). These beam profiles have been recorded at the W2T wire chamber, located in a position where the beam has the maximum (almost maximum) beam size in the x (y) coordinate upstream of B1.

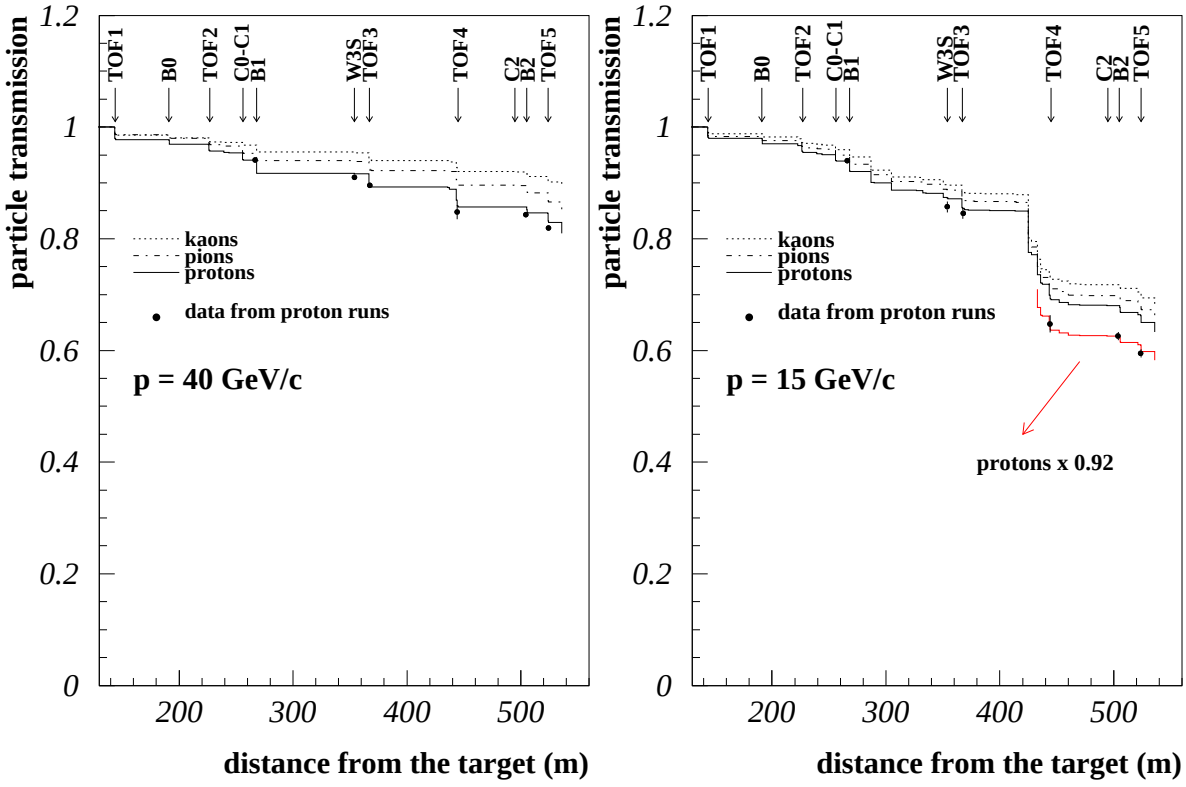

Figure 4: Particle losses downstream of the momentum bite defining collimator. The transmission measured in a dedicated proton run is compared to the results of the TURTLE simulation, for positive particles. At p=15 GeV/c, in the final 150 m of the beam, a rescaled TURTLE simulation curve which fits the data is shown to indicate the magnitude of the systematic error from the discrepancy.

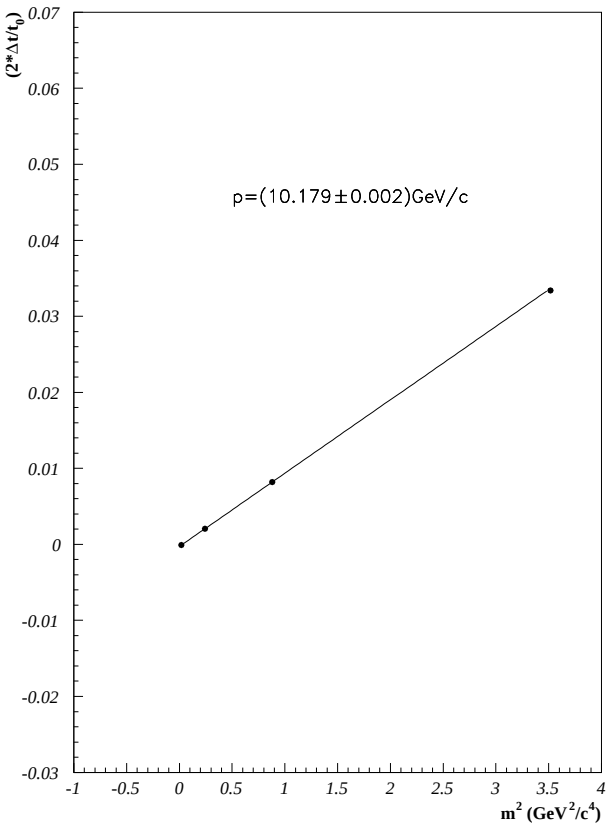

Figure 5: Determination of the momentum for a typical run at a rigidity p/z=+10 GeV/c, using information from the TOF system. The average time delay Δt of massive particles, with respect to $\beta = 1$ particles has been computed from TOF3-TOF1 distributions. It is plotted (multiplied by $2/t_0$) versus the nominal particle mass shift m^2 with respect to the reference one (the pion). The momentum is determined from the fitted slope (see text for details).

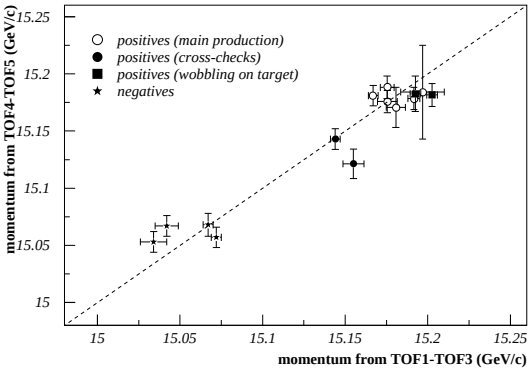

Figure 6: Beam momentum estimates for different runs from time of flight in part B versus part A of the spectrometer at 15 GeV/c. The two runs labelled "cross-checks" have been taken a few days later with a different beam tuning, to check the apparatus stability.

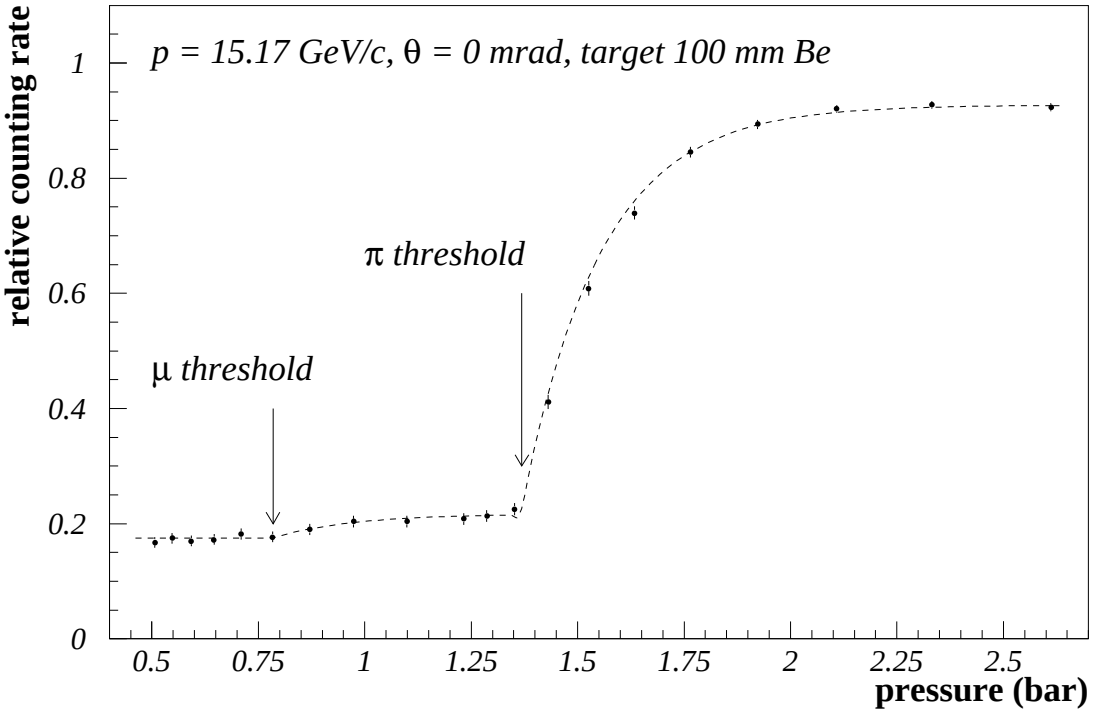

Figure 7: Pressure scan with the C2 threshold counter at 15 GeV/c. The dashed line shows a fit to the experimental points with a threshold at one photoelectron. The μ and π thresholds are clearly visible as well the electron plateau at low pressures. The electron content in the beam is about 20%, while the μ content is around 6%.

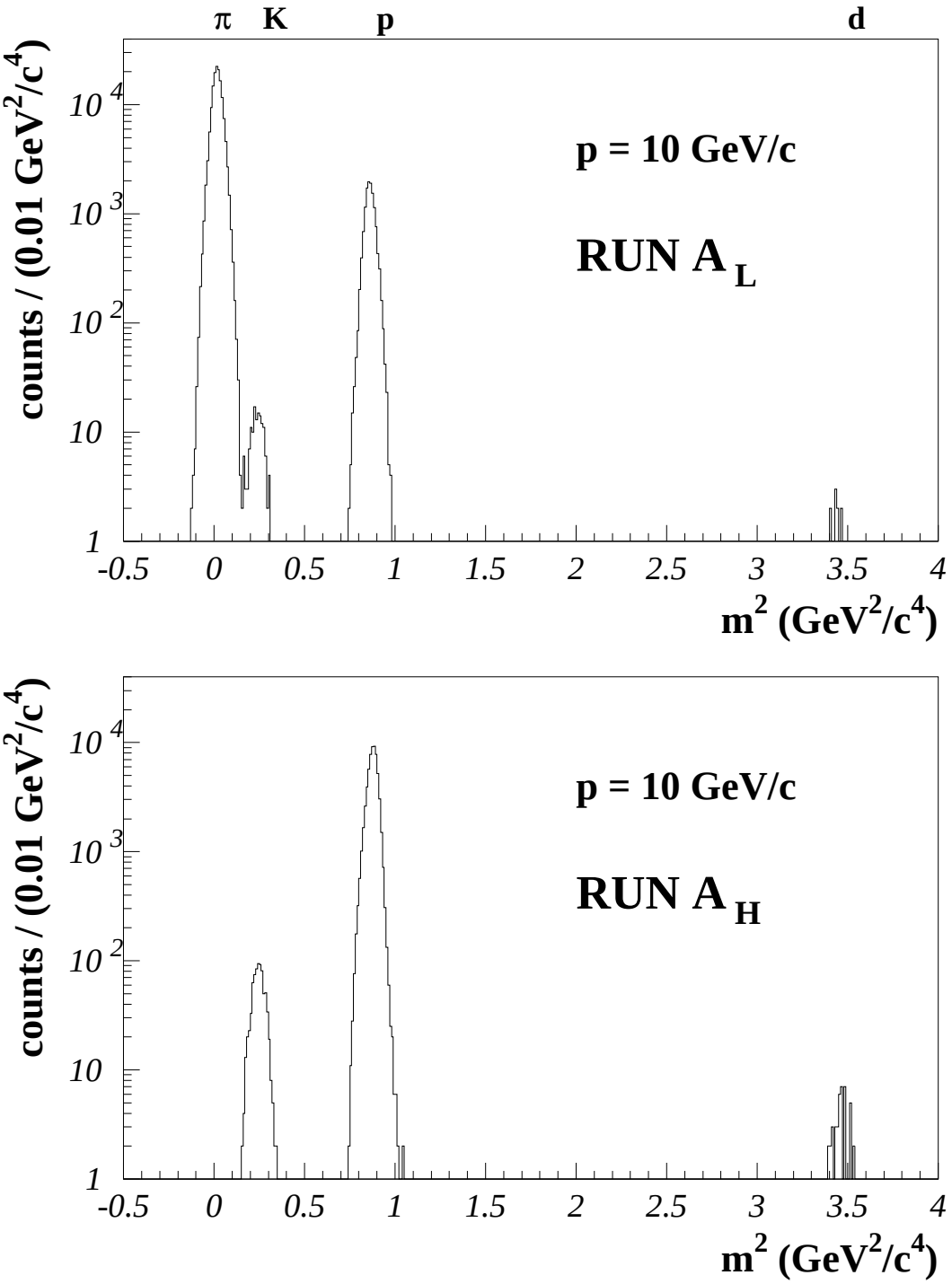

Figure 8: Mass identification from TOF's fit (up to TOF3) at a rigidity p/z = +10 GeV/c

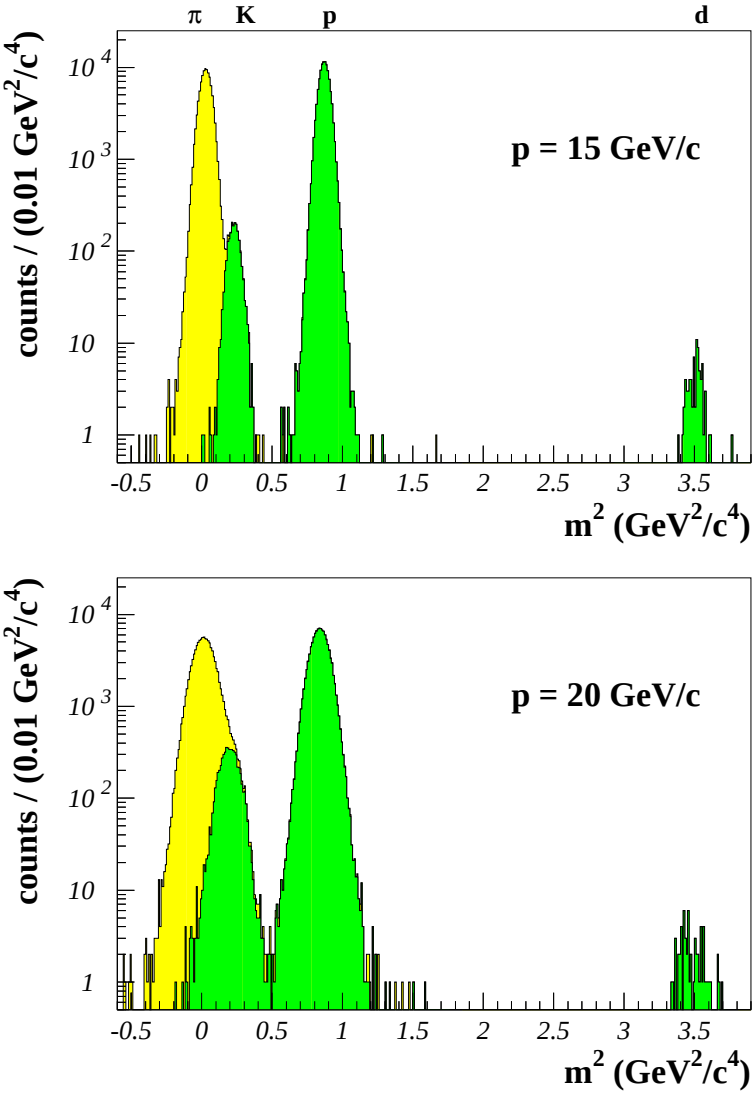

Figure 9: Squared mass spectra at 15 GeV/c (top) and 20 GeV/c (bottom). π/heavy particle separation, as performed from the C0-C1 Cherenkov counters, is superimposed.

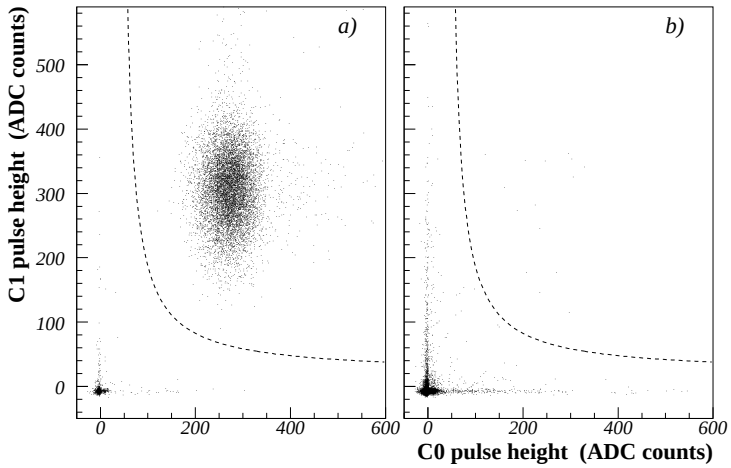

Figure 10: Pulse height spectra observed at 15 GeV/c in the C0 and C1 counters with the $Cveto$-off trigger condition (reflecting the natural beam composition). All the events are shown in (a); while protons cleanly identified by the time of flight information are shown in (b). The dotted curve shows the π/heavy particle separation.

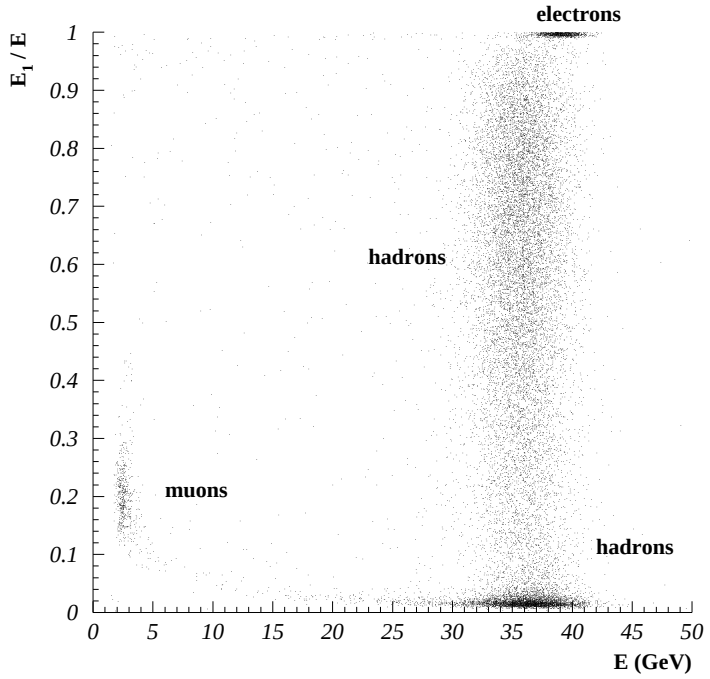

Figure 11: The fraction of the energy deposition E_1/E in the first module of the calorimeter as a function of the total energy E at 40 GeV/c. Muon, electron and hadron interactions are easily identified.

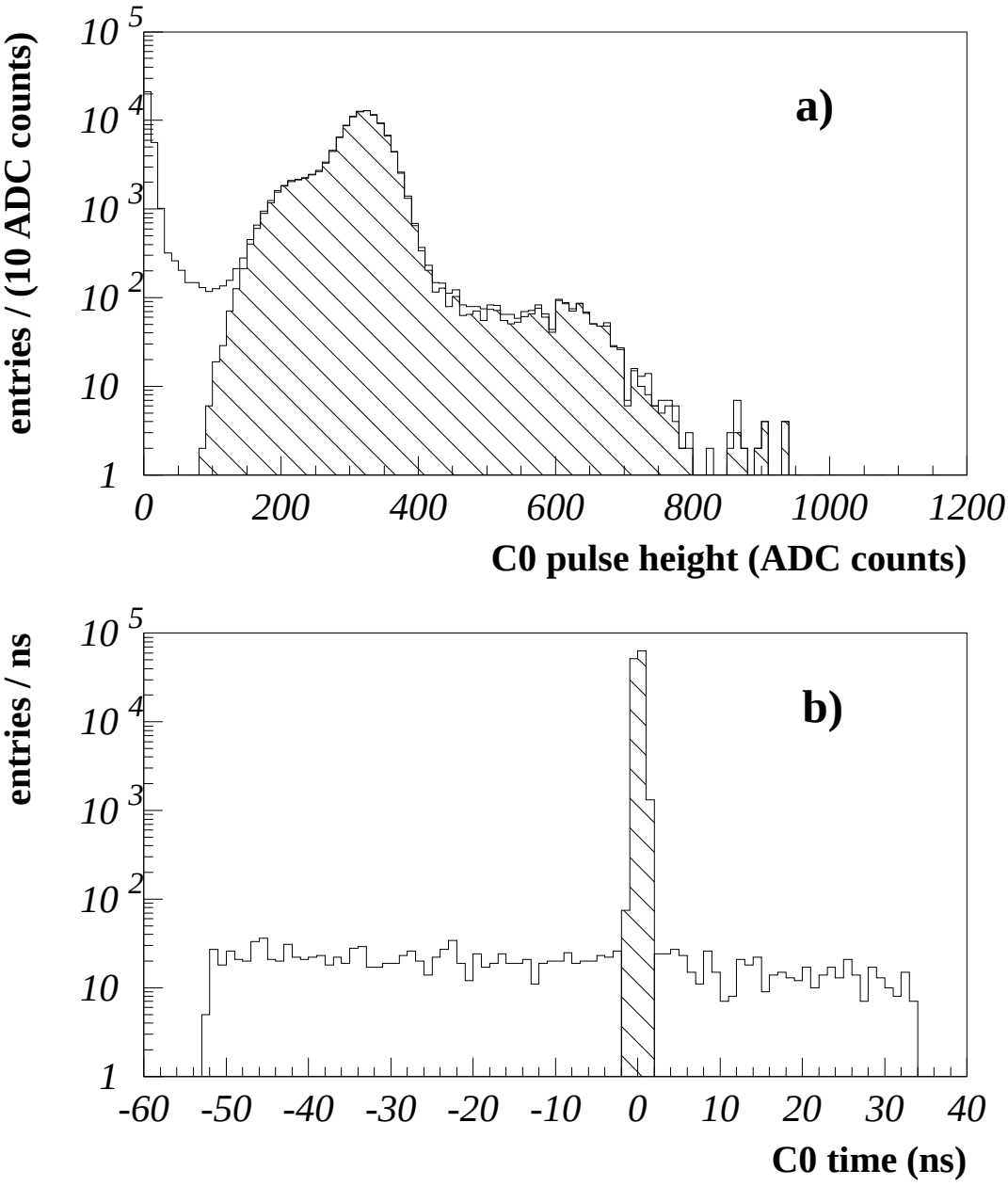

Figure 12: The pulse height (a) and the corresponding time distributions (b) of the signals recorded by the $C0$, counter at 40 GeV/c. In-time events are shaded. The large pulse height tails are due to pileup.

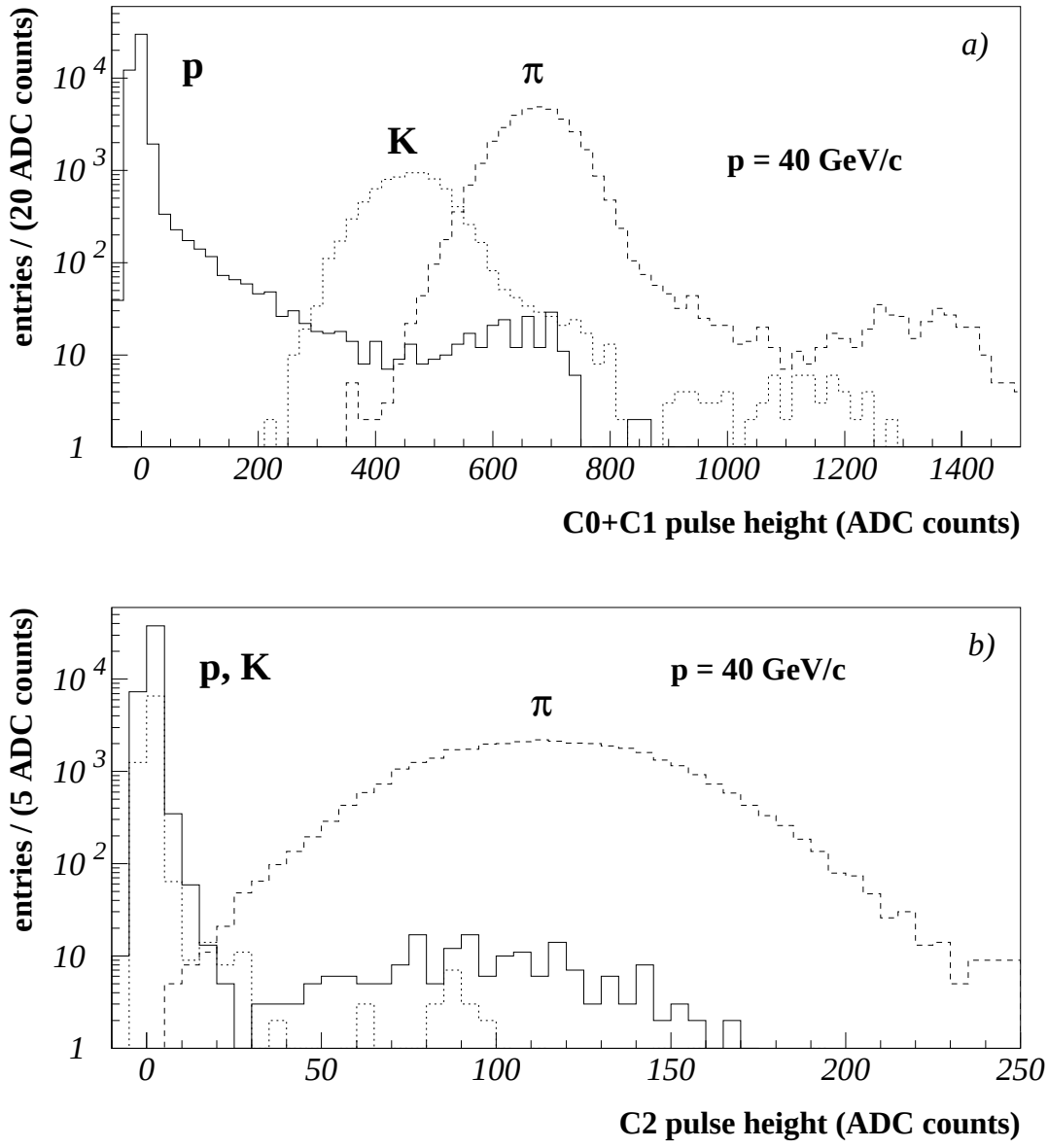

Figure 13: C0-C1 and C2 counter pulse heights, for a typical run at 40 GeV/c. For each kind of particle, secondary peaks in the pulse height spectra are visible. These were interpreted as due to light particle pileup.

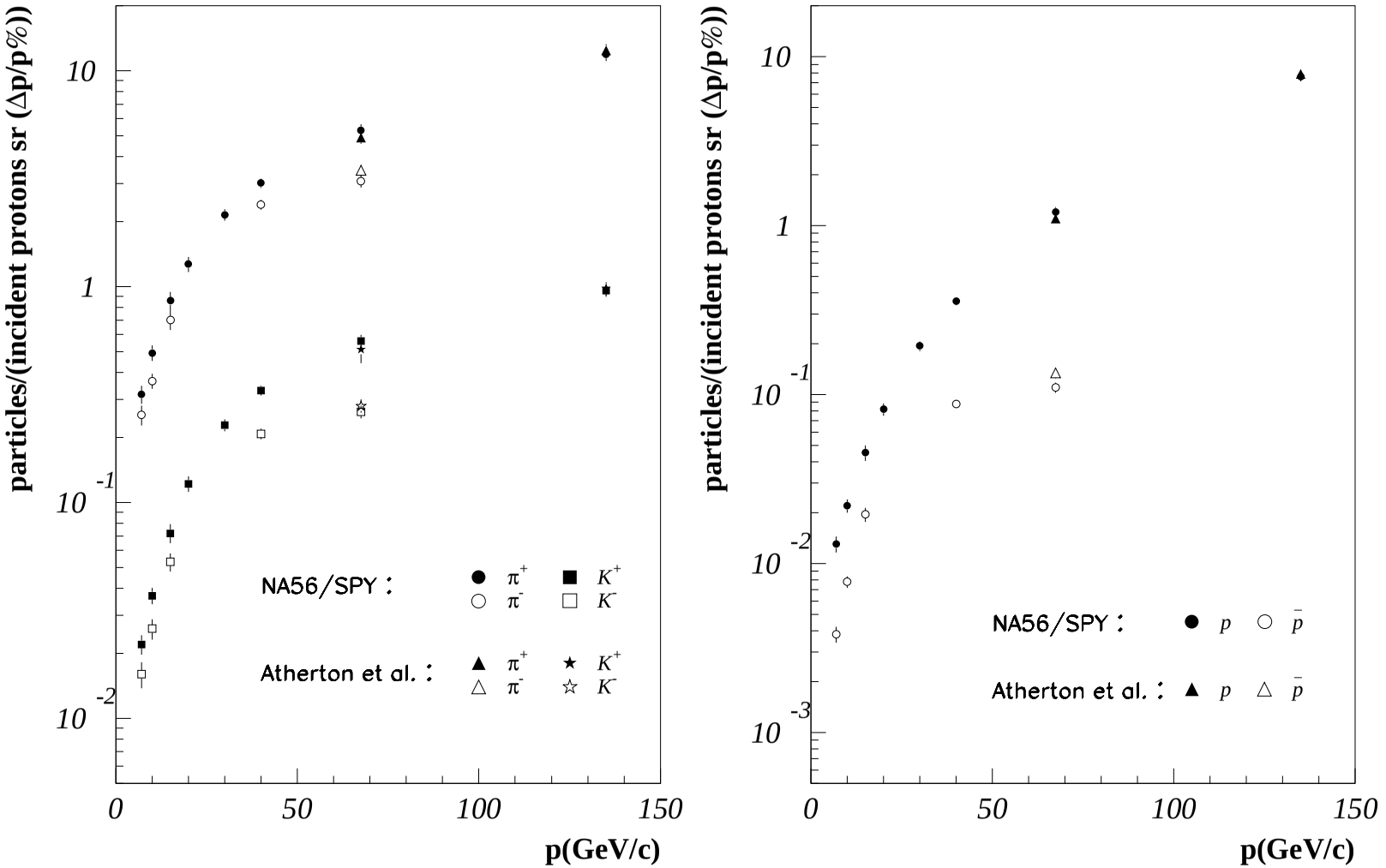

Figure 14: Particle yields in the forward direction for the 100 mm Be target, as a function of momentum. NA56/SPY data are corrected for the contribution of strange particle decays.

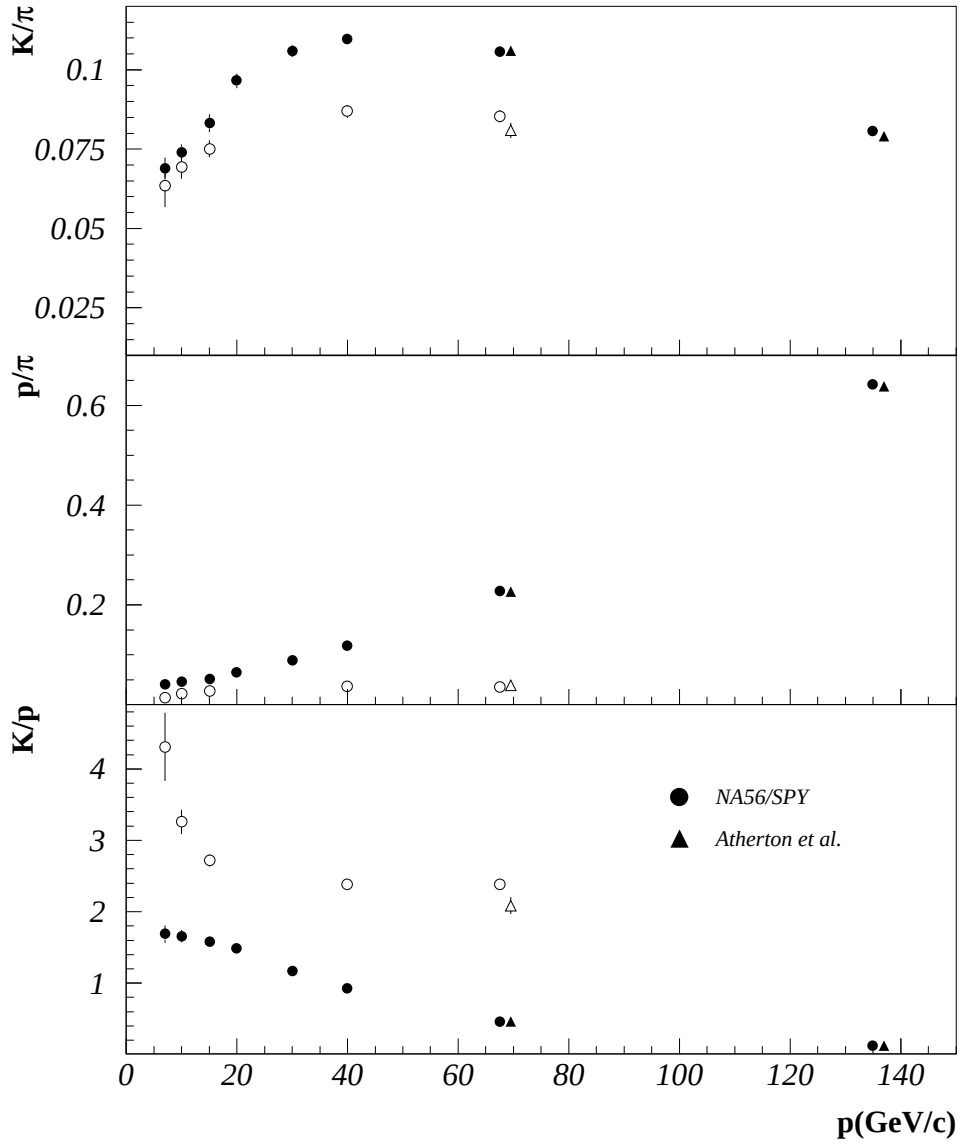

Figure 15: K/π, p/π, K/p production ratios for the 100 mm Be target, in the forward direction, as a function of momentum. Open (full) dots refer to negative (positive) particles. The NA56/SPY data are corrected for the contribution of strange particle decays. Atherton *et al.* are displaced by 2 GeV/c along the momentum axis to make symbols visible.

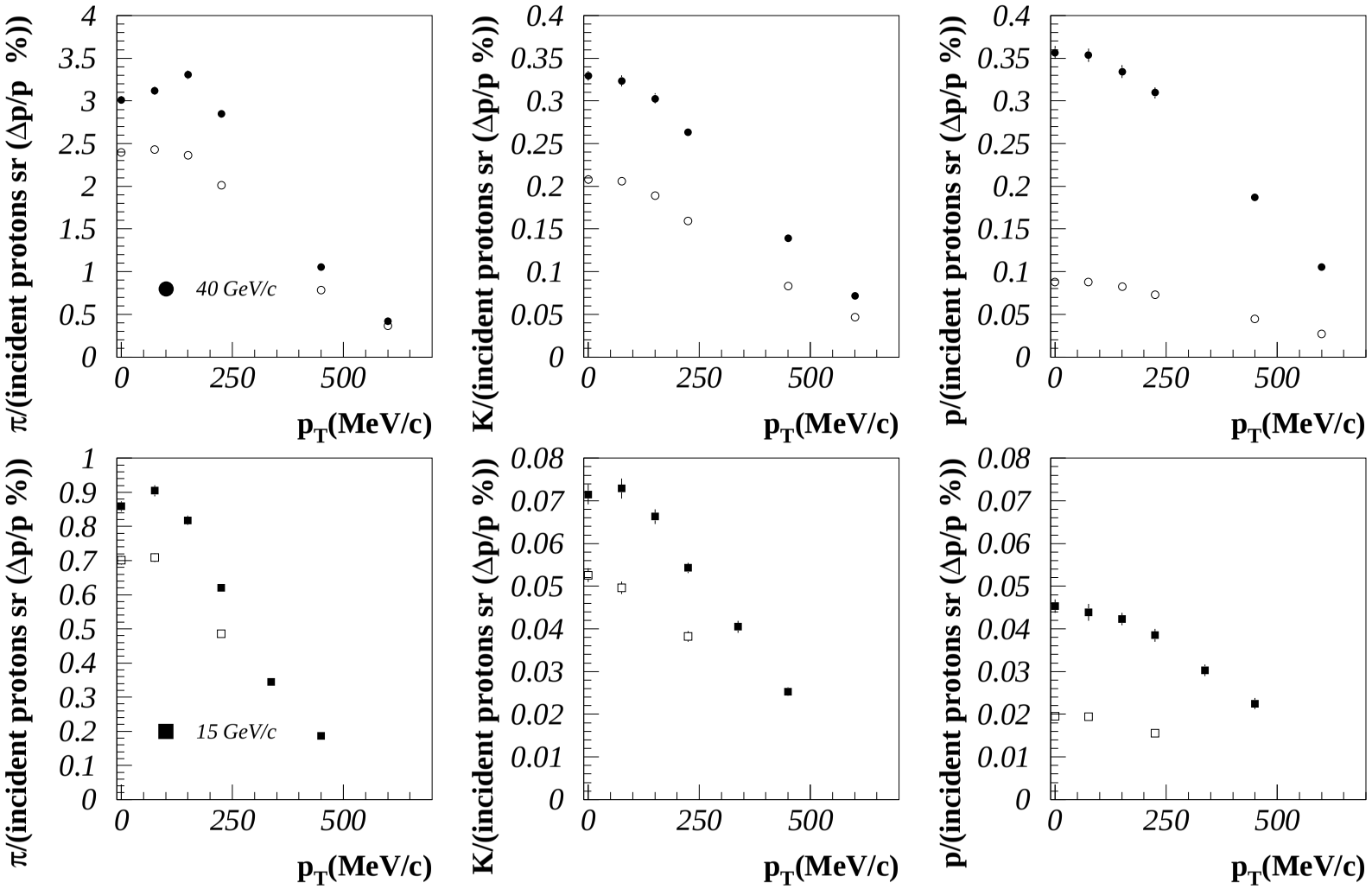

Figure 16: Particle yields at 40 and 15 GeV/c for the 100 mm Be target, as a function of the transverse momentum. Open (full) dots refer to negative (positive) particles. Data are corrected for the contribution of strange particle decays. Common systematic errors are not included.

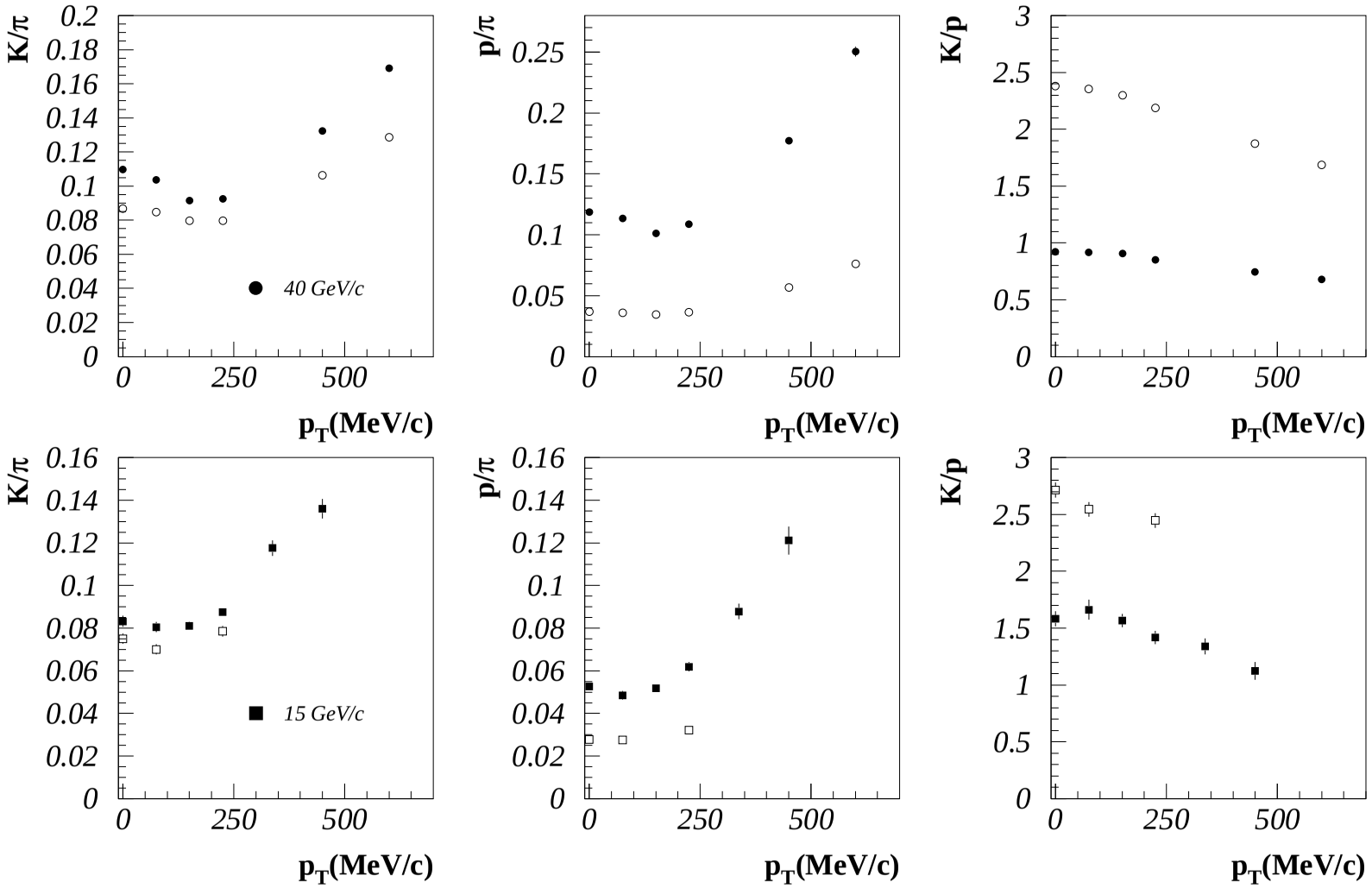

Figure 17: Particle production ratios at 40 and 15 GeV/c for the 100 mm Be target, as a function of the transverse momentum. Open (full) dots refer to negative (positive) particles. Data are corrected for the contribution of strange particle decays. Common systematic errors are not included.

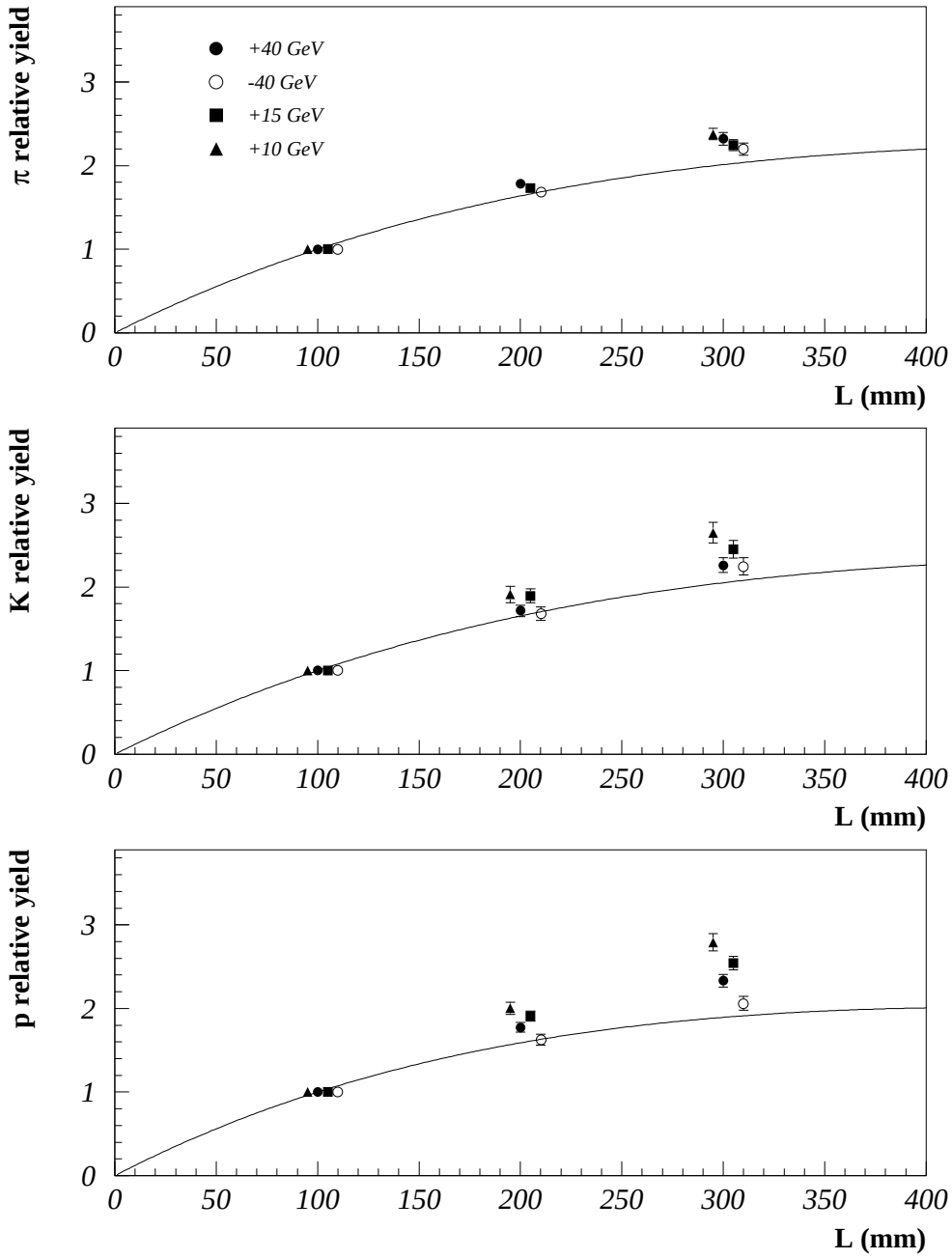

Figure 18: Yields from Be plate targets of length L relative to the 100 mm target for positive (10, 15, 40 GeV) and negative (40 GeV) secondary particles. The continuous line is the prediction of the naive absorption model. Data at rigidities +10, +15 and -40 GeV have been shifted with respect to their nominal position (defined by data at +40 GeV).

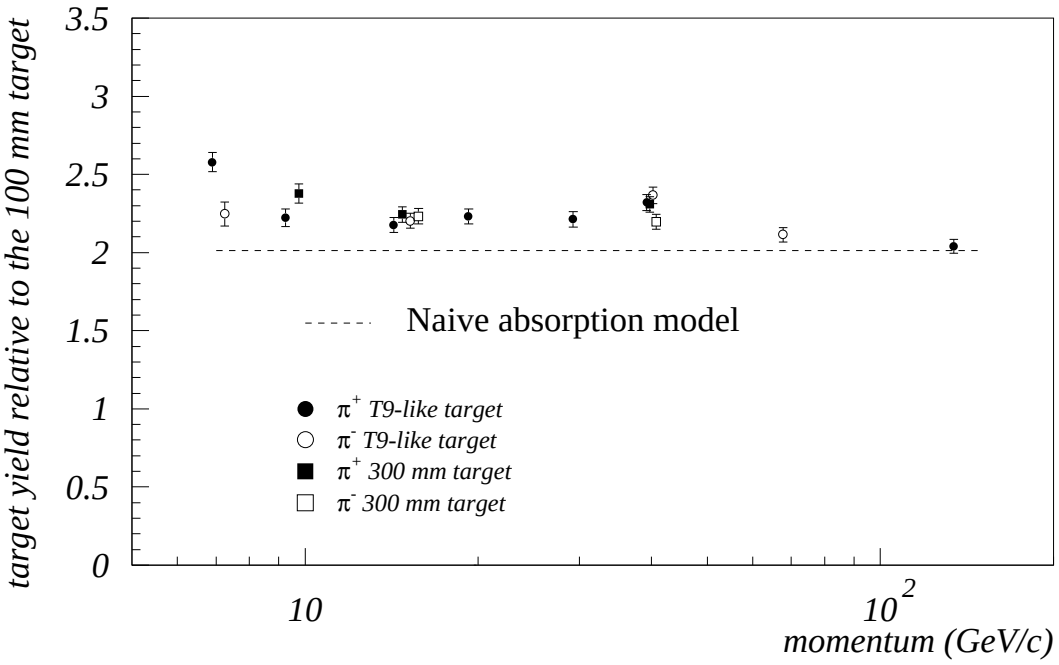

Figure 19: Target yield relative to the 100 mm target as a function of the secondary particle momentum. The dotted line shows the prediction of the naive absorption model.

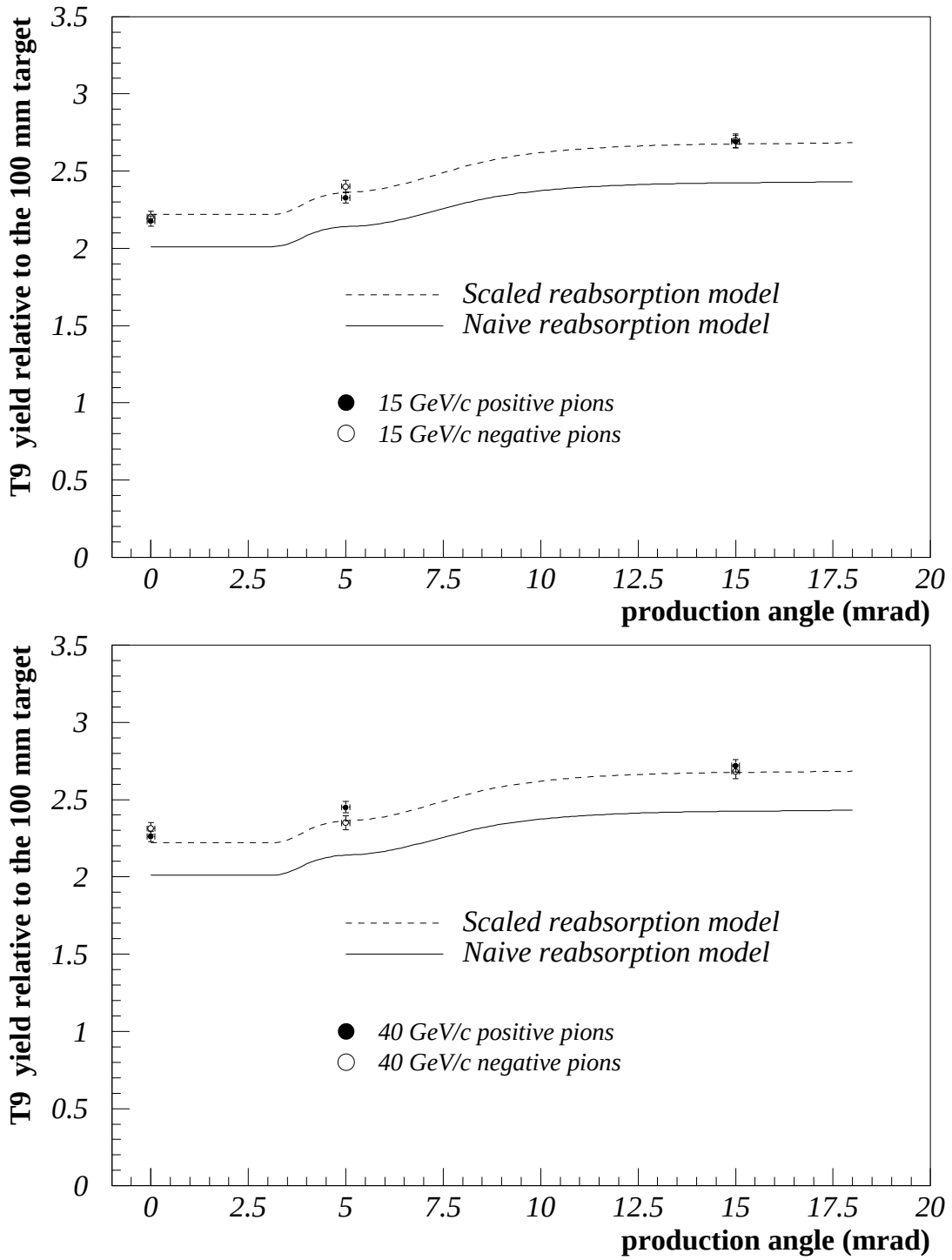

Figure 20: T9-like target yield relative to the 100 mm target as a function of the production angle for 15 GeV/c pions (top) and 40 GeV/c pions (bottom). The full line shows the prediction of the generalized naive absorption model discussed in the text; the dotted line is obtained by rescaling the prediction of the naive absorption model to match the efficiency observed in the forward direction with the 300 mm standard target.

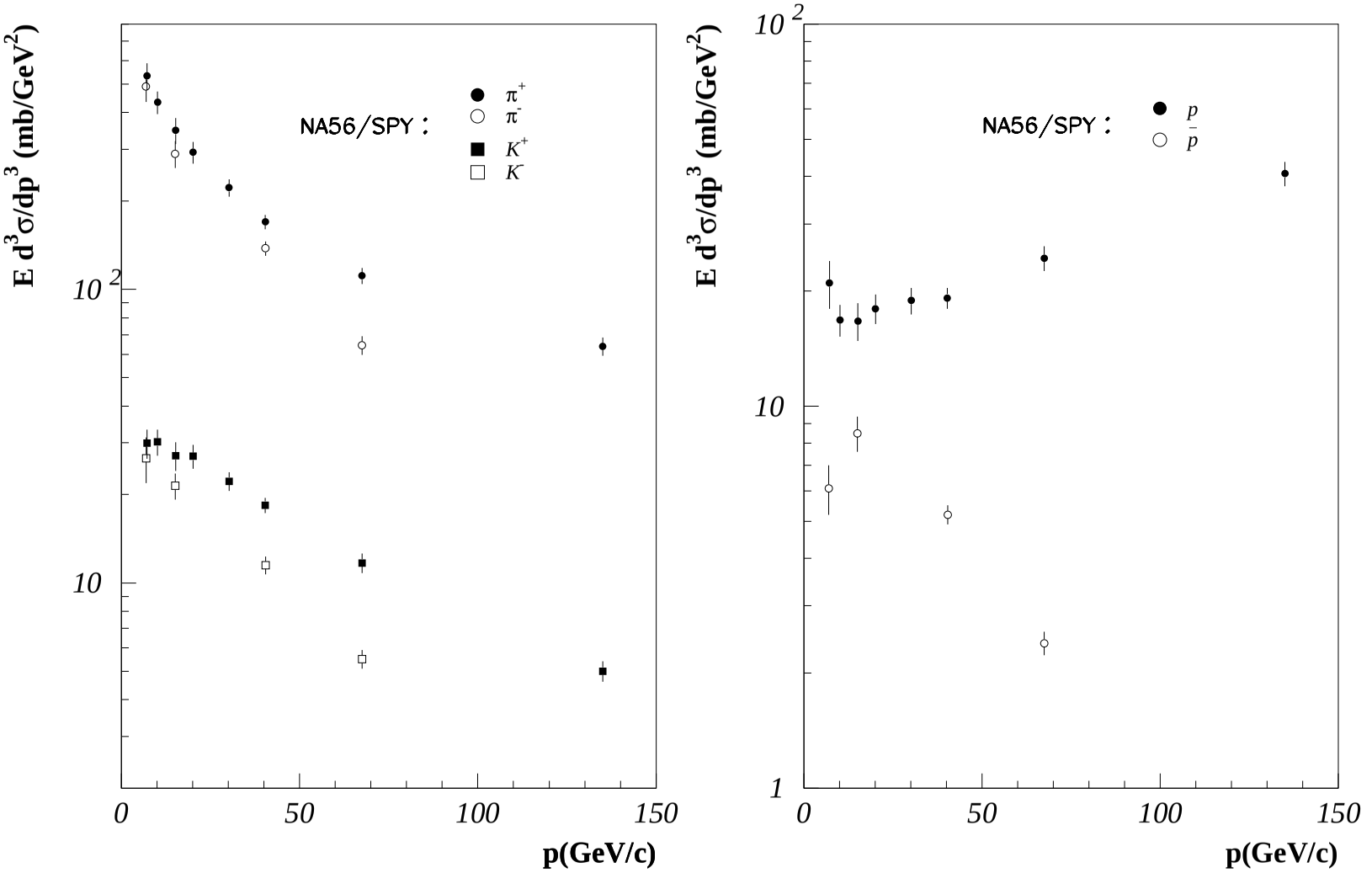

Figure 21: Inclusive invariant cross section as a function of secondary momentum for p-Be interactions at 450 GeV/c in the forward direction.